Visual Abstract

Crashworthiness performance of the designed concave hexagonal structures as filler element in cylindrical shells in multiple load cases

Andre Hartawan Mettanadi, Aditya Rio Prabowo*, Bambang Kusharjanta
Department of Mechanical Engineering, Universitas Sebelas Maret, Surakarta 57126, Indonesia
hartawanandre@student.uns.ac.id
aditya@ft.uns.ac.id, http://orcid.org/0000-0001-5217-5943
bambang_k@staff.uns.ac.id, http://orcid.org/0000-0002-0194-3268

Teguh Muttaqie
Research Center for Hydrodynamics Technology, National Research and Innovation Agency (BRIN), Surabaya 60112, Indonesia
teguh.muttaqie@brin.go.id, http://orcid.org/0000-0002-8850-8313

Fajar Budi Laksono
Department of Research and Development, P.T. DTECH Inovasi Indonesia, Salatiga 50742, Indonesia
fajar@dtech-engineering.com, http://orcid.org/0000-0002-8038-1979

Haris Nubli
Department of Marine Design Convergence Engineering, Pukyong National University, Busan 48513, South Korea
harris@pukyong.ac.kr, http://orcid.org/0000-0002-8976-0107

ABSTRACT. Safety Impact resistance is defined as the ability of a material to absorb impact energy through a controlled failure mechanism. The greater the energy absorption by the crash safety structure, the greater the safety in preventing deformation of the main structure due to impact. Based on the data provided by Statista, in 2020 there were 2,395 people died in road accidents in Italy, that number is still high, so we need vehicle components that are able to protect us from the effects of collisions so that the passengers can be protected. In this study, numerical validation, mesh convergence studies, and multiple load case studies were performed to investigate crash resistance of crashworthiness structure under axial loading. Numerical validation results showed that the similarity between this study and the reference reaches 95%. A deviation of 5% occurred due to different input material properties. The results showed that the concave hexagons as filling elements had greater energy absorption capacity than conventional hollow tubes, and the more concave hexagonal structures, the better the energy absorption. Oblique compression was performed in this study, and as a result, the sample had good impact resistance at low angles and no effect at high

Citation: Mettanadi, A. H., Prabowo, A. R., Kusharjanta, B, Muttagie, T., Laksono, F. B., Nubli, H., Crashworthiness performance of the designed concave hexagonal structures as filler element in cylindrical shells in multiple load cases , Frattura ed Integrità Strutturale, 65 (2023) 135-159.

Received: 29.03.2023
Accepted: 21.05.2023
Online first: 30.05.2023
Published: 01.07.2023

angles like 20°. Therefore, this research aims to improve multi-cell structures for the energy absorption.

KEYWORDS. Energy absorption, Crashworthiness, Thin-walled structures, Multi-cell, Concave hexagonal.

INTRODUCTION

Due to its outstanding mechanical properties coupled with its lightweight and high-performance, the thin-walled structure has been widely applied in various fields, one of which is the crashworthiness of vehicles which can be seen in Fig. 1. During a collision, the occupants of the vehicle experience a number of forces that can result in injuries, including rapid damage and rapid acceleration, depending on the direction of an impact during the collision. Effective crashworthiness vehicle design will distribute these detrimental forces over a long period and distance, including by directing them to parts of the body that are better able to withstand them.

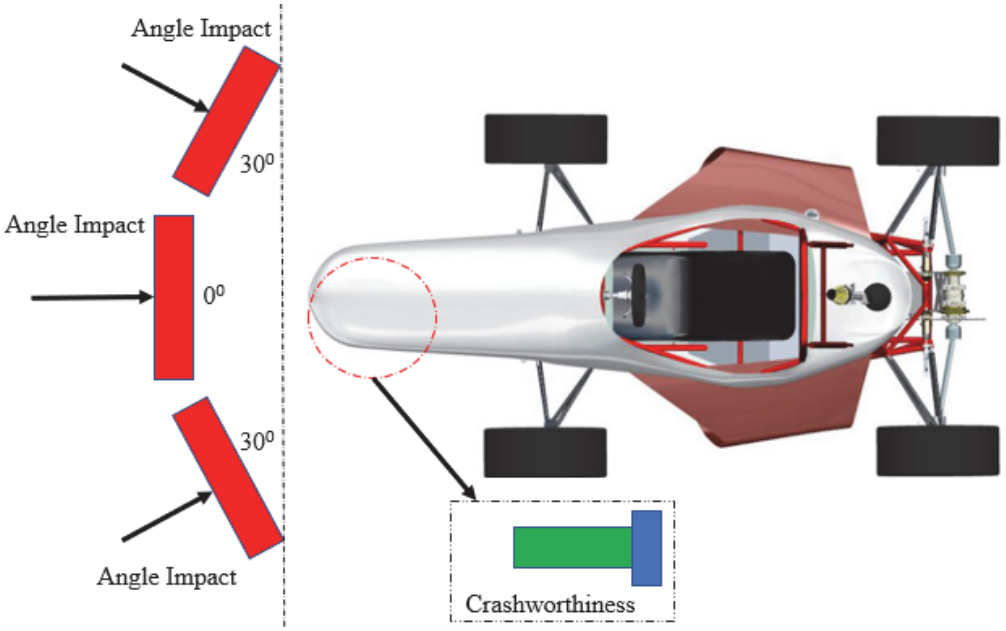

Figure 1: Illustration of crashworthiness in a vehicle.

Single-cell structures with different cross-sectional properties and different shapes and material distributions have been studied intensively in the last few decades, e.g., square structures [1–4], circular geometries [5–8], sinusoidal [9,10], polygons [11,12], and for metal composite hybrid materials [13–16], and many others. With the development of automatic driving technology, there is frequent damage to the occupants and the vehicle's main structure due to many unexpected damage scenes. In recent years, many researchers have tried to increase the impact strength of thin-walled structures [17–22]. To improve the feasibility of thin-walled structures, multicellular energy-absorbing structures combining unicellular and cellular structures have been proposed, which have attracted great attention from researchers due to their better impact resistance compared to conventionally used tubes [23–28]. Several studies have shown that increasing the number of cells in a thin-walled structure can significantly increase the energy dissipation capacity [29–31].

The multi-cellular structure was developed by combining cellular and unicellular arrangements to increase the impact resistance of thin-walled structures. Kim [32] proposed a new multi-cell box arrangement by optimizing the distribution of box elements in the corners. The results show that the collision resistance of the new multi-cell profile is almost twice that of the original structure. Vinayagar et al. [33] proposed the triangular shape of the tube into a circular tube, resulting in a two-part multicellular column with a more stable deformation pattern than the traditional unicellular structure. Optimization of the configuration of the multicellular fallopian tube structure was proposed by Sun et al. [34]. Compared with the original

tube, the optimized results show more energy absorption under axial and inclined impact conditions. The above studies confirm the performance advantages of multi-cell structures over single-wall columns in many respects, but there is still room for improvement in their energy efficiency.

The above studies confirm the performance advantages of multi-cell structures over single-wall columns in many respects, but there is still room for improvement in their energy efficiency. So in this study, we aim for the improvement of the multi-cell aspect applied to the structure. We choose the concave hexagonal structures with a given number of cores and the effectiveness of the object when it is hit from various angles, namely 0°, 10°, 20°, and 30°. Therefore this research is expected to be useful for optimizing the crashworthiness structures in a crash box for the safety component in a vehicle.

LITERATURE REVIEW

In-land vehicle accident: sample data

With the increasing population in a region, it will also impact the need for transportation facilities. This can boost the sale of motorized vehicles such as cars and motorbikes or the increase in users of public transportation facilities such as buses. On the other hand, with the increasing volume of vehicles on the highway, it will also be more prone to driving accidents. This is certainly not what we want. Based on the data provided by Statista [35]. The number of accident victims in Italy experienced an overall downward trend from 2006-2020, as seen in Fig. 2. In 2020, just under 2,400 individuals were killed in car accidents in Italy, down from more than 3,000 in 2019. This was the lowest value on record since the peak in 2006 due to the pandemic of Covid-19 and travel restrictions in the country. Many situations of accidents occur due to drowsiness, the influence of alcohol, and others that cause the vehicle to hit an object, and the structure of the vehicle is still not able to reduce the force due to the collision, so that passengers experience the impact and become injured. Based on the picture, car accidents in Italy are still high, above 2000 fatalities in 2020 or approximately 199 cases per month.

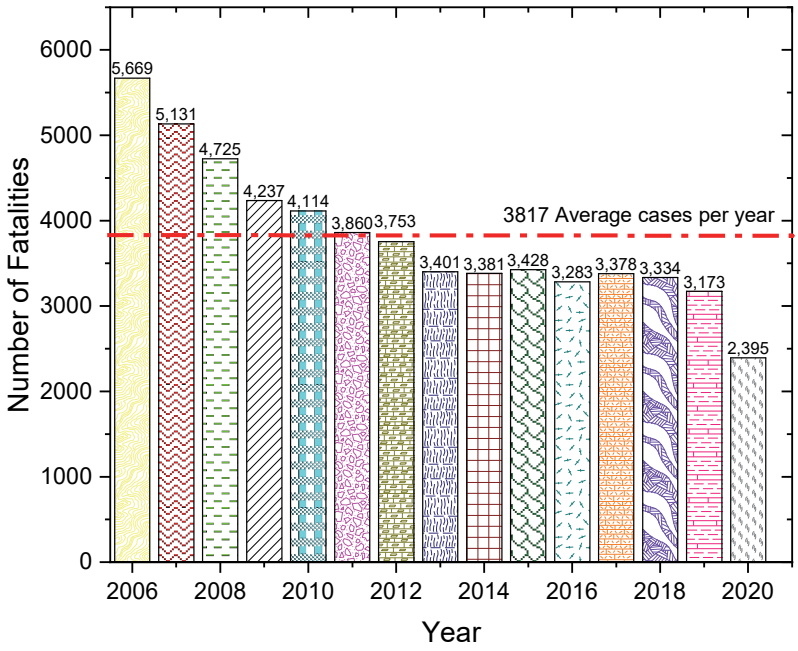

Figure 2: Number of road fatalities in Italy from 2006-2020.

The development of automotive technology has an impact on the need for driving safety systems, such as the example of an airbag system in a car that protects passengers from hitting the vehicle interior during a collision with sensor technology. Still, this technology does not protect the vehicle's main frame, and a bad situation can occur if this sensor is inactive or does not work properly. Therefore, a vehicle component is needed that can absorb the collision energy experienced by the vehicle itself to protect the passengers inside and the car's main structure. Crash boxes that contain the crashworthiness structure of the vehicle are considered capable of reducing the force of the collision so as not to endanger the passengers inside or the main chassis of the vehicle.

Indicator of structural crashworthiness

The force transfer diagram, as shown in Fig. 3, is the most common and widely used indicator of crashworthiness, by showing the relationship of compressive strength to the maximal thin-walled profile (PCF) strength contraction and sample contraction during the breaking process, which is the basis for the energy dissipation development plot [36]. Tarlochan et al. [37] described the peak forces, Fmax, and energy absorption (EA) in a thin-walled structure subjected to axial and oblique impact forces. The peak force of a component is the maximum load required to cause significant permanent deformation of the body. In simulation, the peak load is measured using the reaction force on a fixed platform.

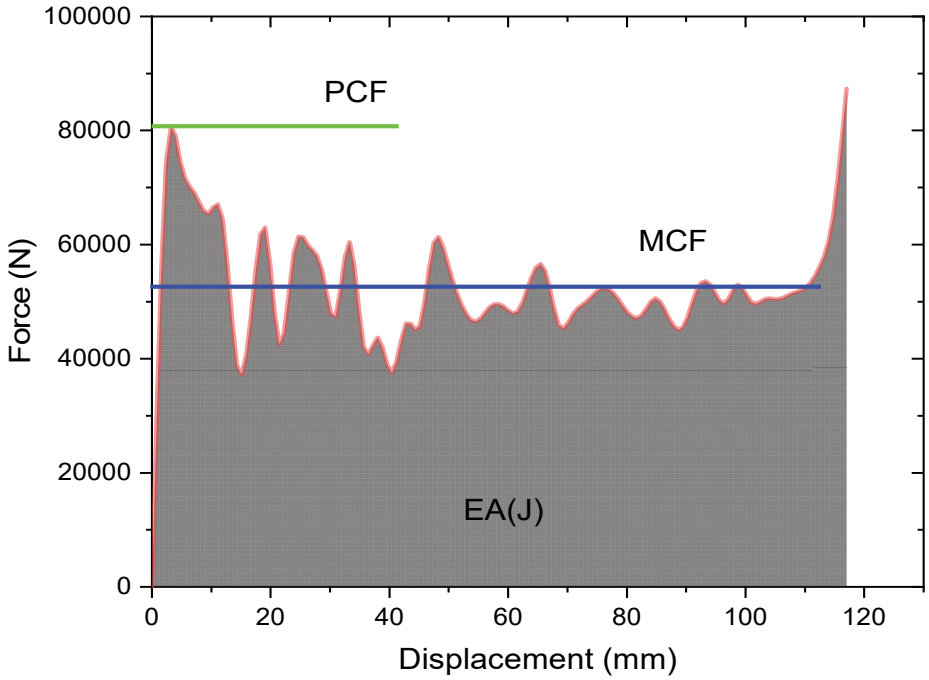

Figure 3: Peak crushing force (MCF), mean crushing force (MCF), and energy absorption (EA) in force vs displacement curve.

Energy absorption and axial deformation caused by axial compressive loads were investigated using a cylindrical cross-section tube. Energy absorption is obtained by first calculating the reaction force/crushing load. Typical failure modes of square tubes laid out by Abramowicz et al. [38] predicted the reaction force/compression load. A higher energy absorption efficiency of a material is reflected in a higher specific energy absorption (SEA) value, as seen in Eqn. 1. The differential energy absorption (SEA) is obtained by calculating the energy absorption per unit mass of the structure as follows:

$$SEA = \frac{EA}{M} \tag{1}$$

$$\eta(d) = \frac{\int_0^d F(x)dx}{F(x)} \tag{2}$$

where EA and M represent the energy absorption of the cylinder and the total mass, respectively. EA is equal to the area surrounded by the force transfer curve as in the example: The cut-off transfer of the energy absorption process is determined according to the energy efficiency method, which is presented in Eqn. 2. In addition, the mean crushing force (MCF) is analyzed as the average energy absorption experienced by the material, which is depicted in Eqn. 3.

$$\eta(d) = \frac{\int_0^d F(x)dx}{F(x)} \tag{3}$$

The value of η(d) represents the energy absorption efficiency. The cut-off displacement (point C), as shown in Fig. 3, is the displacement value corresponding to the stationary point (point A) where global efficiency is maximum. The SEA

corresponding to point C is the total specific energy absorption. While the MCF represents the mean or average crushing force from the curve shown in Fig. 4 from the yield point to the broken material. Considering the influence of the impact angle on the impact resistance of the structure of the object, two comprehensive indicators and were developed to evaluate the impact resistance of structures under multi-angle loading, which is defined as [39]:

$$SEA_{\varnothing} = \sum_{k=1}^{N_\theta} \omega_{\theta_k} \; SEA_{\theta_k} \tag{4}$$

$$PCF_{\varnothing} = \sum_{k=1}^{N_\theta} \omega_{\theta_k} \; PCF_{\theta_k} \tag{5}$$

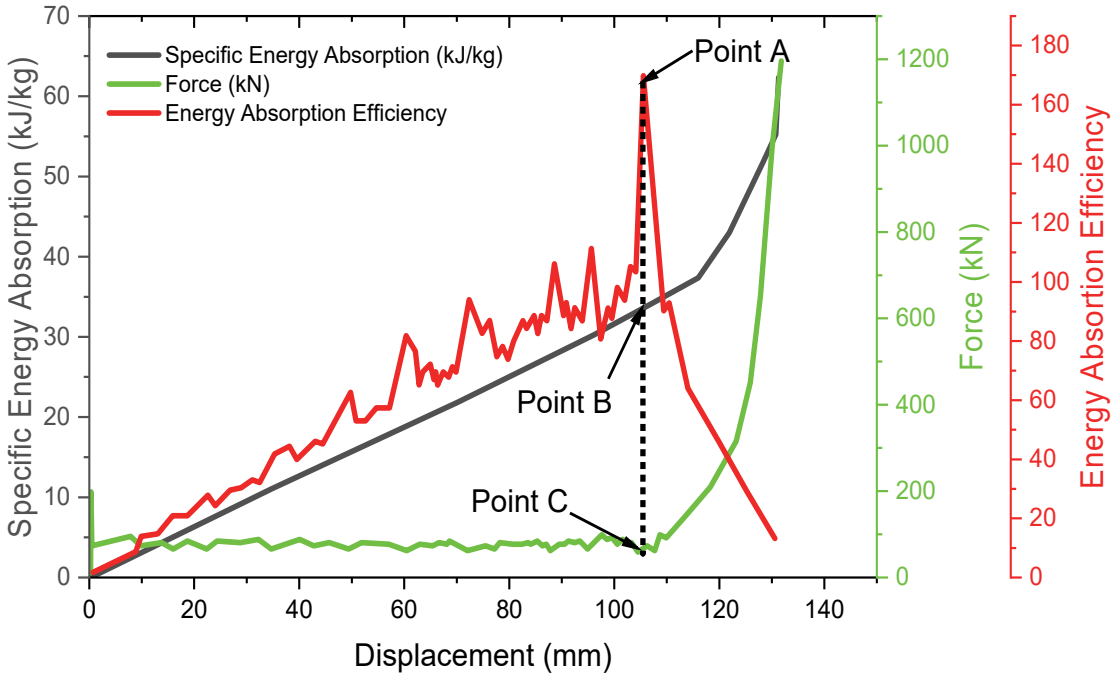

Figure 4: Schematic of deriving crashworthiness indicators [40]. Point A is the position where the energy absorption efficiency is a global maximum. The displacement value corresponding to the stationary point (point A) is the cut-off displacement (point C). The SEA value corresponding to point B is the total SEA at the cut-off displacement.

Fundamentals in finite element analysis

Incremental loads are required for all nonlinear and non-static analyses. Simply put, solving a math problem requires breaking down the relationship between physics and time. We usually use "implicit" and "explicit" methods to solve these problems. Implicit and explicit problems are expressed by mathematical partial differential equations. Today's computers cannot solve his PDE on their own, but they do have the ability to solve matrix equations. These matrix equations can be linear or nonlinear. For most structural problems, nonlinear equations fall into three categories.

Material Nonlinearity: where deformations and strains are large (i.e., polymer materials),

Geometric Nonlinearity: where strains are small, but rotations are large (i.e., thin structures),

Boundary Nonlinearity: due to non-linearity of boundary conditions, (i.e., contact problems).

In linear problems, the PDE's reduce to a matrix equation as:

$$[K]\{x\} = \{F\} \tag{6}$$

and for non-linear static problem as

$$[K(x)]\{x\} = \{F\} \tag{7}$$

For Dynamics, the matrix equation comes down to:

$$[M]\{\ddot{x}\}+[C]\{\dot{x}\}+[K]\{x\}=\{F\} \tag{8}$$

[M], [C], [K] - Mass matrix, damping matrix, and stiffness matrix, respectively
$[\ddot{x}],[\dot{x}],[x]$ - Acceleration, Velocity, and Displacement, respectively
[F] - Load Vector

One method of solving for the unknowns {x} is through matrix inversion (or equivalent processes). This is known as an *implicit analysis*. When the problem is nonlinear, the solution is obtained in a number of steps, and the solution for the current step is based on the solution from the previous step. For large models, inverting the matrix is highly expensive and will require advanced iterative solvers (over standard direct solvers). Sometimes, this is also known as the backward Euler integration scheme. These solutions are unconditionally stable and facilitate larger time steps. Despite this advantage, the implicit methods can be extremely time-consuming when solving dynamic and nonlinear problems. *Explicit analysis* aims to solve for acceleration (or otherwise $\{\ddot{x}\}$). In most cases, the mass matrix is considered as "lumped" and thus a diagonal matrix. Inversion of a diagonal matrix is straightforward and includes inversion of the terms on the diagonal only. Once the accelerations are calculated at the nth step, the velocity at n + 1/2 step and displacement at n + 1 step are calculated accordingly. In these calculations, the scheme is not unconditionally stable; thus, smaller time steps are required. To be more precise, the time step in an explicit finite element analysis must be less than the Courant time step (i.e., the time taken by a sound wave to travel across an element), while implicit analyses have no such limitations. Therefore, we use dynamic explicit non-linear method because it is time dependent and the condition is really fast with the velocity is 15000 mm/s, because automotive crash causes an increasing in the strain rate.

Dynamic-explicit algorithm

Explicit dynamics is a time integration method used to perform dynamic simulations when speed is important. Explicit dynamics account for quickly changing conditions or discontinuous events, such as free falls, high-speed impacts, and applied loads. In this case the situation is high-speed impact, the dynamic explicit simulation was carried out using ABAQUS [41]. The authors argue that the simulation of thin-walled structures subjected to compressive loads is part of the dynamic wake. Pioneer works using dynamic finite element, e.g., [42-52] presented the deployed algorithm implemented in collision and grounding simulations. The dynamic equilibrium equations of the system are:

$$M\ddot{u}(t)+f(t)-p(t)=0 \tag{9}$$

$$\ddot{u}_n = M^{-1}\left[p_n - f(u_n)\right] \tag{10}$$

$$\ddot{u}_n = \frac{\dot{u}_{n+1/2} - \dot{u}_{n-1/2}}{\frac{1}{2}(\Delta t_n + \Delta t_{n+1}} \tag{11}$$

$$\dot{u}_{n+1/2} = \frac{u_{n+1} - u_n}{\Delta t_{n+1}} \tag{12}$$

The value of is the nodal displacement vector, while M represents the mass matrix, f, and p are the internal force and external load vectors, respectively, where t stands for time. Then, for velocity and displacement, calculation can use from Eqn. 11 and Eqn. 12, respectively, with a central differential operator. Using the values obtained from the previous time steps, we know that the solution progresses with time, namely the velocity and the displacement. Due to the limited time addition, this scheme is only conditionally stable. This clear solution strategy is highly efficient and suitable for describing general contact conditions and considering large rotations and stresses to model crushing and tearing. This is because there is no iteration and there is no need to formulate a stiffness matrix for axial and shear forces. The peak load of a component is the maximum load required to produce significant permanent deformation. The peak load is the highest value of the reaction force received by the test object. Fig. 3 shows the force transfer diagram. The total energy absorption can be plotted for the pre-cracked and progressively fractured regions of formed samples/structures with different masses.

RESEARCH METHODOLOGY

Problem description

Axial and angular collisions are the two main points of vehicle collision, as shown in Fig. 1. In previous studies, many experts have intensively studied key components with bionic structures to increase vehicle impact resistance, such as energy dampers and front springs. These studies have achieved excellent results in ideal axial impact scenarios, but little attention is paid to tilt effects. In this section, high-precision simulation models were built and verified with reference results and numerical results. This study comprehensively investigated the proposed new cylinder rods by considering the axial and oblique impact cases. Assuming that the bottom face of the cylinder was attached to a rigid base plate and compresses a rigid plate moving with an initial speed of 15000 m/s and a constant mass of 600 kg at the top of the cylinder. The acceptable compression angle between the rigid plate and the test sample varied from 0° to 30°.

Geometrical model

We declared the current test specimen with "Cyl-1" name. In this study, a numerical model was created using 3D CAD software then to investigate the compression characteristics of Cyl-" in various loading cases using the nonlinear explicit dynamic ABAQUS software. For this purpose hexagonal structures were prepared as fill elements for the cylindrical shell specimens as shown in Fig.. 4, which were divided along the circumference and radial directions of the cylindrical shell and connected by circular arcs. It was assumed that the outer diameter of the inner diameter is represented by **d** and **D**. The coefficient α was used to express the ratio between the two diameters, namely **α = d/D**. The number of concave hexagons in the perimeter and radial distributions was indicated by **x** and **y**, respectively. As shown in Fig.. 5, the cylindrical shell has a uniform thickness distribution t = 1 mm. The sub-parameters x, y, and α were 6, 2, and 0.5, respectively. The axial height of the cylindrical shell was 150 mm and the outer ring diameter was 60 mm.

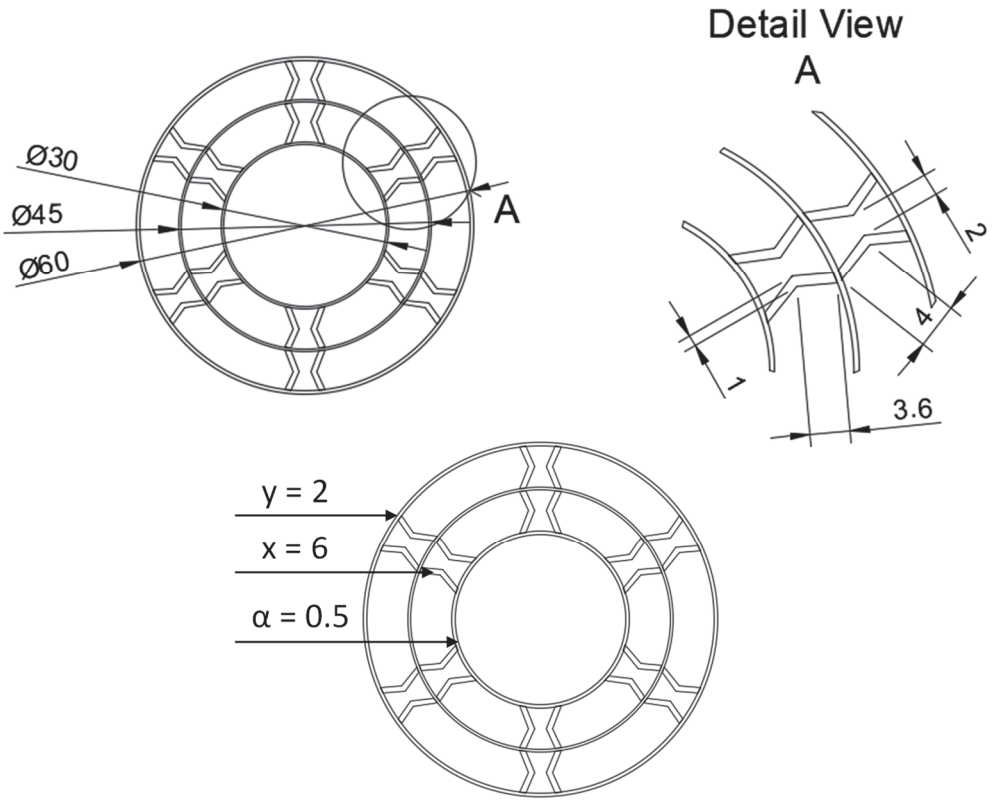

Figure 5: Details of the geometrical model Cyl-1.

Finite element settings

In this section, a finite element configuration was given to analyze the performance of Cyl-1 under axial impact conditions. For the geometric elements used, a homogenous continuum shell element type was used, these shell types are general-purpose shells that allow finite membrane deformation and large rotations and, thus, are suitable for nonlinear geometric

analysis. These elements include the effects of transverse shear deformation and thickness change with uniform thickness t = 1 mm. The cylindrical shells had the same axial height of 150 mm and had an outer ring diameter of 60 mm. The sub-parameters m, n, and α were 6, 2, and 0.5, respectively. The dimensions of the hexagonal concave cross-section of sample "Cyl-1" can be observed in Fig. 5. As for the contact properties given in the form of hard contact, the "hard" contact relationship minimized the penetration of the slave surface to the master surface at the constraint location and did not allow tensile stress transfer across the interface. Then, "Tangential Behaviour" was given with a penalty type with a friction coefficient of 0.2. Simulating ideal friction behavior can be very difficult; therefore, in most cases, ABAQUS uses a penalty friction formulation with allowable "elastic slip" by default. "Elastic slip" is the small amount of relative motion between surfaces that occurs when the surfaces are supposed to stick. ABAQUS automatically selects the penalty stiffness (slope of the dashed line) so that this allowable "elastic slip" is a very small part of the characteristic element length. The penalty friction formulation works well for most problems, including most metal-forming applications.

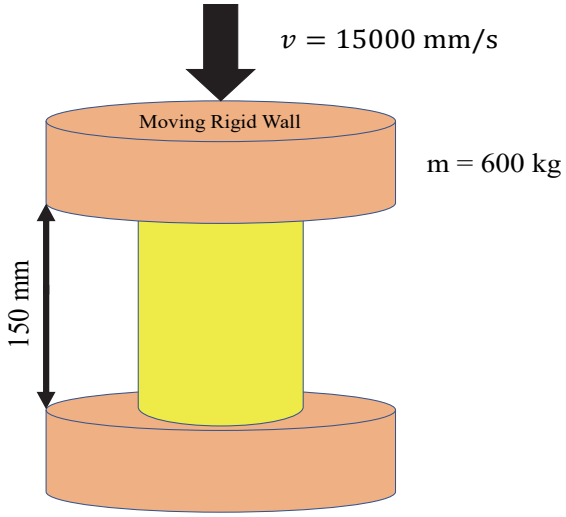

Figure 6: Schematic illustration of the idealized compression test.

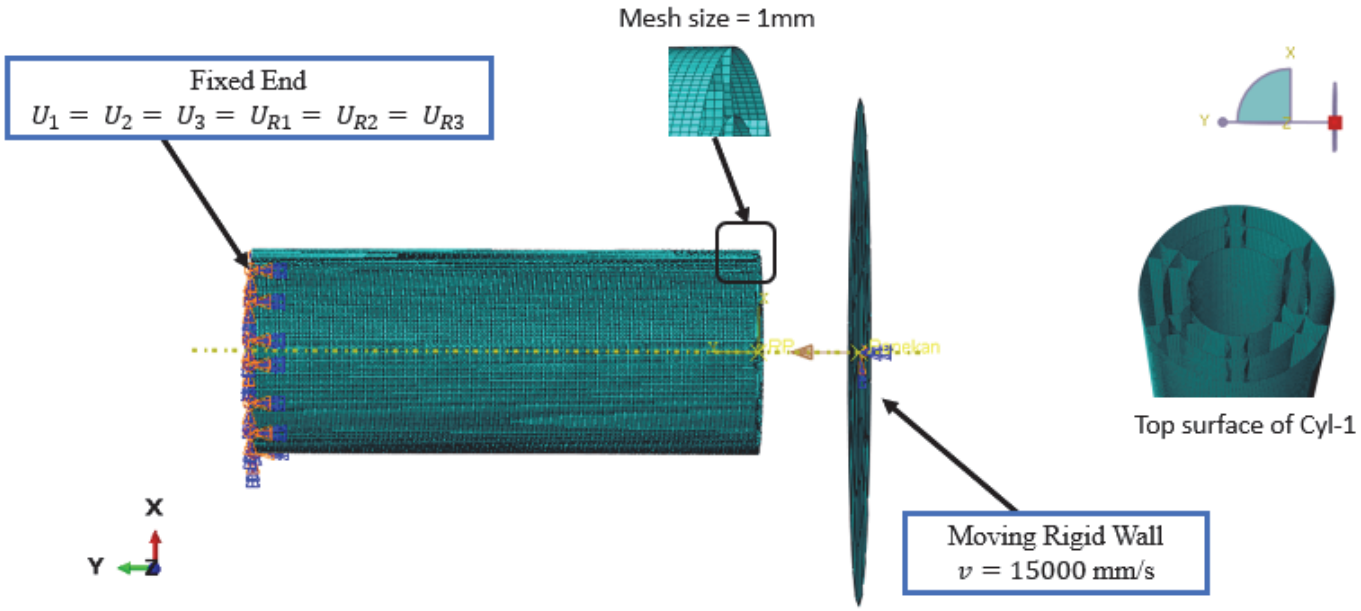

Figure 7: Boundary condition settings for Cyl-1.

The boundary conditions can be observed from the illustration in Fig. 7. The upper surface of Cyl-1 was compressed by a rigid wall that moves at an angle of 0°. The mass of the moving rigid wall was 600 kg described as an inertia mass. On the

lower surface, Cyl-1 was limited to the fixed end (U_1= U_2= U_3= U_{R1}= U_{R2}= U_{R3} = 0) which is shown in Fig. 7. The upper part had a horizontal velocity limit condition. The specified velocity control for the Cyl-1 FE model was 15000 mm/s axially described as an initial speed. The cylindrical shell used S4R element / Quad elements with reduced integration and finite membrane strain, this means the cylindrical shell had four nodes with quadrilateral elements, with the global size of 1 mm. For the indenter, it was described as 3D discrete rigid elements, this means the indenter assumes to be rigid and cannot deform with the mesh element size of 21 mm globally.

Material properties

Various impact resistance studies have been carried out using alumunium as the base material for the sample, some of which are, for example, Jafarzadeh and Schroder [53] who studied impact resistance using Alumunium 6060 as the base material. The next example is Rogala et al. [36] who used 6061-T6 alumunium as the base material for conical energy dampers, and others such as Zarei and Kroger [54] who studied impact resistance with foam-filled alumunium. Based on these studies, alumunium is used because it is lighter than other metals such as steel but has quite strong properties. Based on the findings of the above studies, the material used in this research is Alumunium 6061-T4, which has the characteristics of high performance and lightweight. The material's properties are shown in Tab. 1 and a stress-strain curve was given so that the relationship between stress and strain in the material can be observed as shown in Fig. 8.

Material Properties	Units	Value
Density	kg / mm^3	2700
Poisson ratio	-	0.28
Young's Modulus	GPa	70
Initial Yield Stress	MPa	112.14
Ultimate Stress	MPa	214.16
Shear Modulus	GPa	260
Shear strength	MPa	170
Thermal Conductivity	W/m.K	170

Table 1: Material properties of Alumunium 6061-T4.

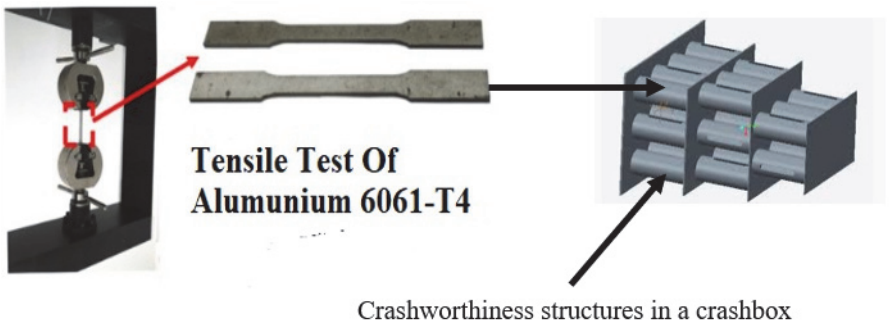

(a)

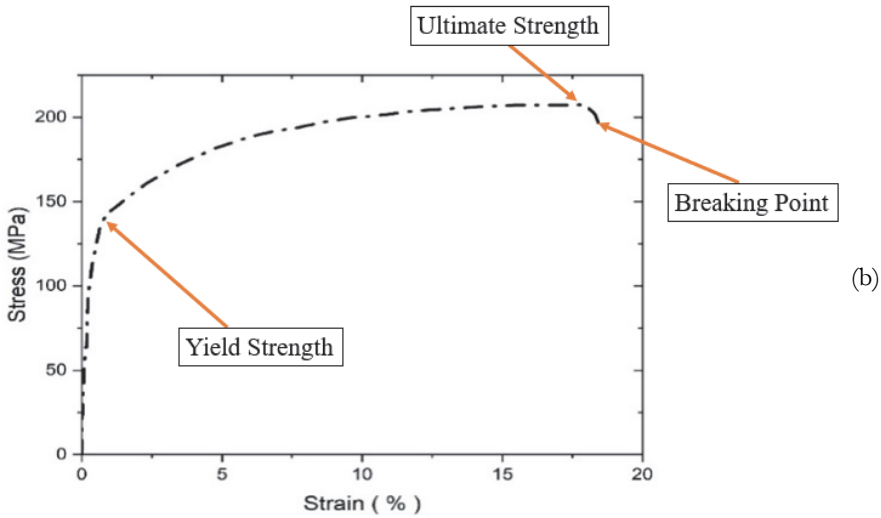

(b)

Figure 8: (a) Tensile test of Alumunium 6061-T4, and (b) Stress-strain relation curve.

Profiles of benchmark particulars

In this research, we used Liang et al. [40] research on specimen named as "BBT-1" for this benchmark of this study, based on research on a new bionic bamboo tube design under several compressive loads that have been carried out by Liang et al. [40]. The base model was tested with a universal testing machine conducted in automotive simulation and control laboratory in Jilin University of Changchun, China it was compressed at room temperature over a measurement range of 300 kN. The name of the tested specimen was "BBT-1", as shown in Fig. 9. The dimension of BBT-1 was same as Cyl-1 as shown in Fig. 4 Next, the alumunium 6061-T4 was compressed by universal testing machine. The testing machine then drilled a hole in the sample by cutting the wire to process the internal cavity of the BBT-1 structure. Then the wire-cutting wire was carried out using computer programming to complete the processing of the BBT-1 test object. The top surface of the BBT-1 sample was placed on a rigid plate and pressed with a moving plate with a pressing speed of 5 mm/min. The results obtained from the compression test of "BBT-1" specimen was used to validate this study as hysterical result later discussed in result of benchmarking study in the result and discussion's section.

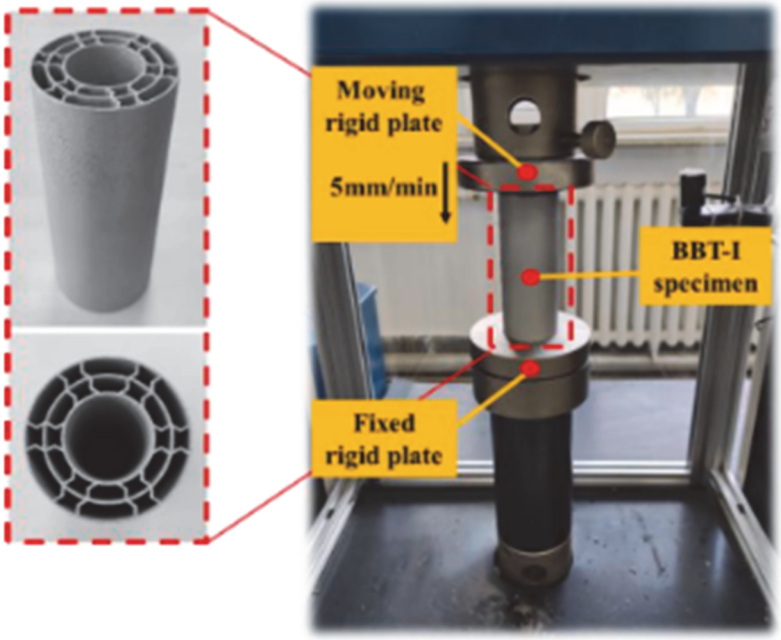

Figure 9: Compression test conducted by Liang et al. [40] on the "BBT-1".

Result and discussions

Results of benchmarking study

After examining the Cyl-1 specimen which had the same geometry model as BBT-1 and with the same boundary conditions applied, it was found that the maximum yield force (PCF) was 92.38 kN. In addition, the average force (MCF Numerical) recorded in Fig. 10 was equal to the energy absorption ratio to the reference MCF, which is "BBT-1". The experimental and simulation average failure values compared with the numerical results obtained were 77.99 kN, 79.12 kN, and 79.09 kN. This result was also confirmed by the line in Fig. 10a, which shows that the lines coincided. The results obtained were close to the benchmark simulation results and slightly higher than the experimental results at an error rate of 5%. Regarding the change trajectories observed in Fig. 10b, it can be seen that the trajectories shown by Cyl-1 and BBT-1 look similar at each step up to 8 ms. It can be seen from the shape of the stress and the shape of the stress that the force received was evenly distributed on the body of the Cyl-1 sample.

Compared with the numerical processing results, The cones formed from the test results obtained by the general testing machine show the similarity in the number of blocks formed up to 8 cones, so it can be concluded that the experimental and numerical results show similar tendency which indicated that the current FE methodology has successfully verified based on comparison with pioneer work of Liang et al. [40]. For the stress and strain contour as seen in Figs. 10c and 10d, respectively, the stresses and the strain seem to be evenly distributed in specimen body.

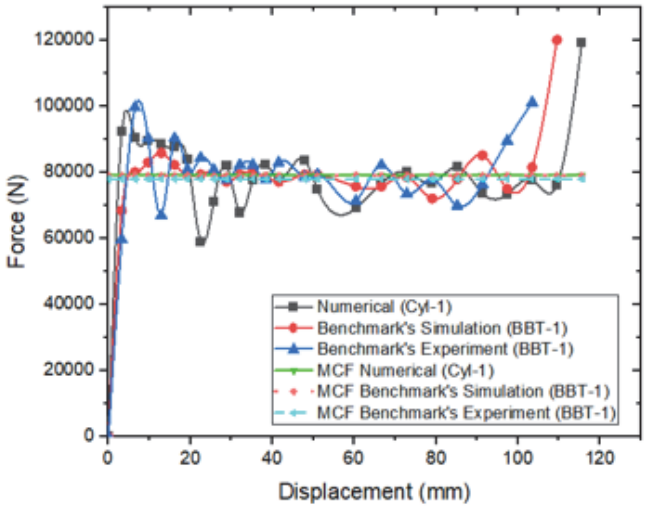

(a) Force -Displacement compared to bechmark's results.

(b) Displacement contours of BBT-1 and Cyl-1.

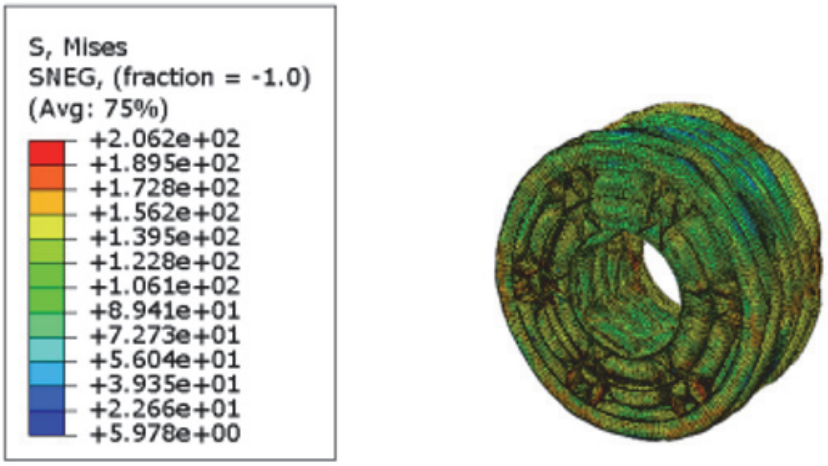

(c) Stress contour of Cyl-1 at 8 ms.

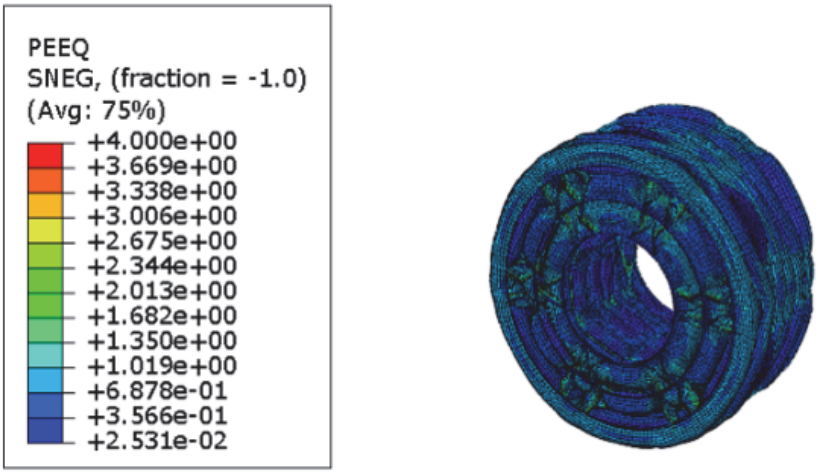

(c) Strain contour of Cyl-1 at 8 ms.

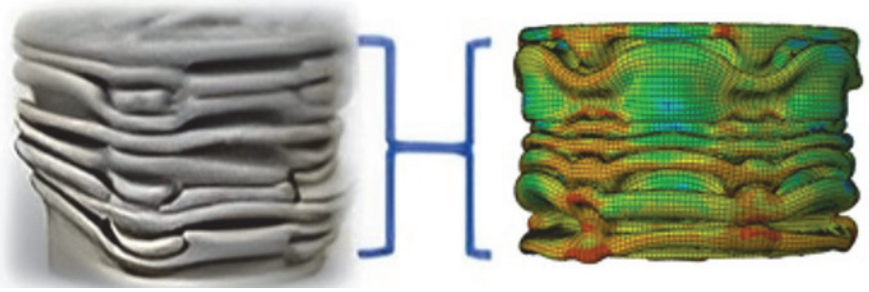

(e) Lobes formed after test (front view): 8 lobes.

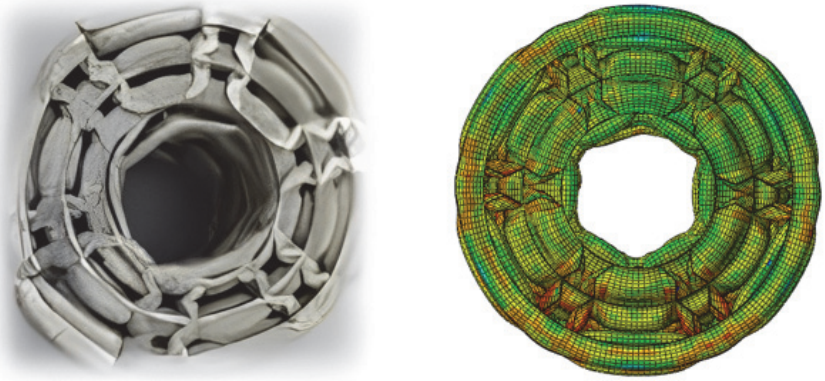

(f) Vertical view of the experimented BBT-1 and numerical results of Cyl-1.

Figure 10: Numerical results and comparisons: (a) Force result compared with benchmark's result; (b) displacement contours of BBT-1 compared to Cyl-1; (c) stress contour at time step 8 ms; and (d) strain contour at time step 8 ms; and (e) Comparison of lobes formed after test. BBT-1 (left) and Cyl-1 (right) (f) Vertical view of the experimented BBT-1 (left) and numerical result of Cyl-1 (right).

Mesh convergence study

To determine the appropriate number and size of mesh for further studies, a convergence mesh study is required. The simulation results are not only influenced by the geometry and material properties but also by the shape and size of the mesh. If the curve is made with the horizontal axis as the number of elements and the vertical axis as the simulation results, a logarithmic curve will usually be formed. The logarithmic curve determines the number of elements and mesh size that

can be used. The determination can be made by looking at the number of elements that have started to appear convergent (if the elements multiplied do not have a large effect on the result).
The results of the convergence mesh curve can be seen in Fig. 11. Specifically, Fig. 11a shows that the greater the number of elements, the smaller the energy absorption. At the number of elements 4320, the value of energy absorption reached 22.03 kJ/kg. This value decreased as the number of elements increased. However, for elements 23402, the energy absorption tended to stabilize at 4.5 kJ/kg. Mesh convergence was achieved at an energy absorption value of 2.87 kJ/kg with a number of elements of 93148. The opposite occurred at displacements, where the greater the number of elements, the greater the displacement that occurs. As can be seen from Fig. 11b, mesh convergence was achieved when the displacement was 108.552 mm with the number of elements 96148. This was further clarified in Fig. 11a which shows that when the element size was 1 mm the progressing displacement tended to be more stable compared to other meshes. Summary of the convergence mesh study from a mesh size of 10 to 0.5 is presented in in Tab. 2. Based on the progress contour that can be observed in Fig. 12, that the mesh size affected the stress and strain experienced by the specimen, for example with a mesh size of 10 mm, the stress experienced tended to be smaller compared to a smaller mesh so that the object looked irregularly deformed at the time step of 4 ms and 8 ms. As for the convergence of 1 mm mesh size, it can be seen that when the time step was 4 ms and 8 ms the object deformed regularly and compared to a larger number of meshes. This indicated that the smaller the mesh size, the more accurate the results will be.

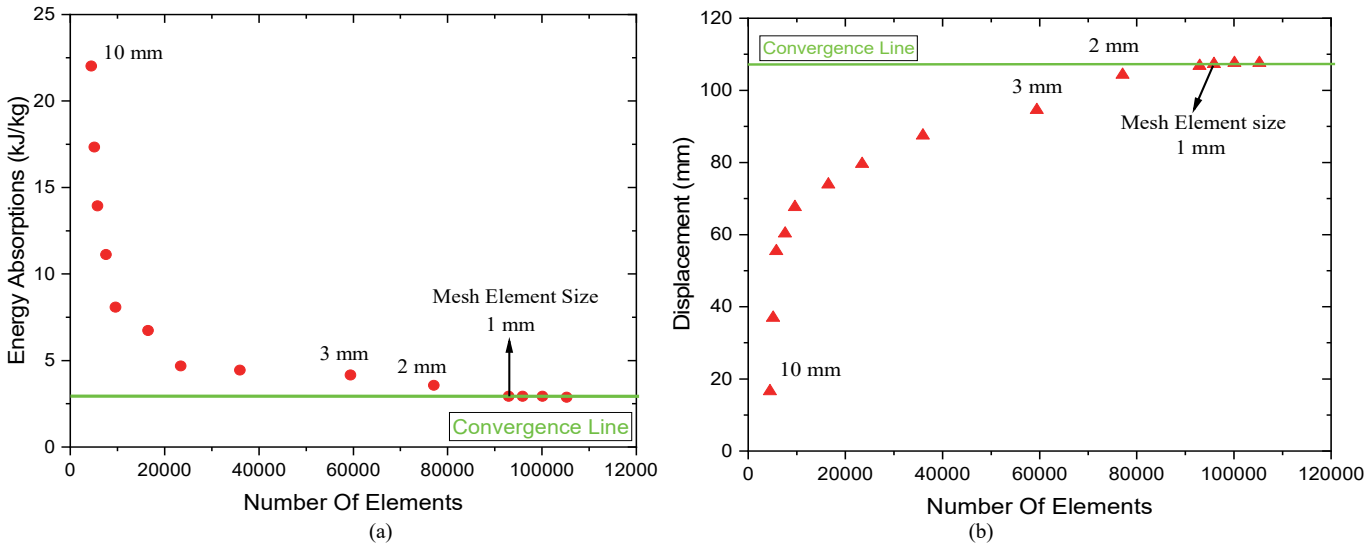

Figure 11: Results of the convergence study based on the given parameters: (a) energy absorption; and (b) displacement.

Parameter	Mesh Size					
	10 mm	5 mm	3 mm	2 mm	1 mm	0.5 mm
Number of elements	4320	23402	59441.34	77094.97	96148	96865.92
Displacement (mm)	94.54	79.59	94.54	104.31	108.522	109.3
Energy absorption (kJ)	22.03	4.5	4.15	3.57	2.87	2.68

Table 2: Mesh convergence study from 10 mm mesh size to 0.5 mm.

Variation of core inside concave hexagonal

As depicted in Fig. 13, this study divided the cross-section of the Cyl-1 specimen into three types, namely: (i) $\alpha = 3$, (ii) $\alpha = 4$, (iii) $\alpha = 5$, (iv) $\alpha = 6$, these specimens had the same boundary condition and material as Cyl -1 except the α and same type of mesh element which was S4R Quad type. After conducting the simulation, it can be seen that the number of cores in the cylindrical shell as a filler element greatly influenced the increase in energy absorption by the cylindrical shell. As can be seen in Fig. 14, there was a significant increase in PCF and MCF. The more the number of cores, the greater the PCF and MCF experienced by these objects due to the increased surface area of the cylindrical shell which was pressed by the moving rigid wall.

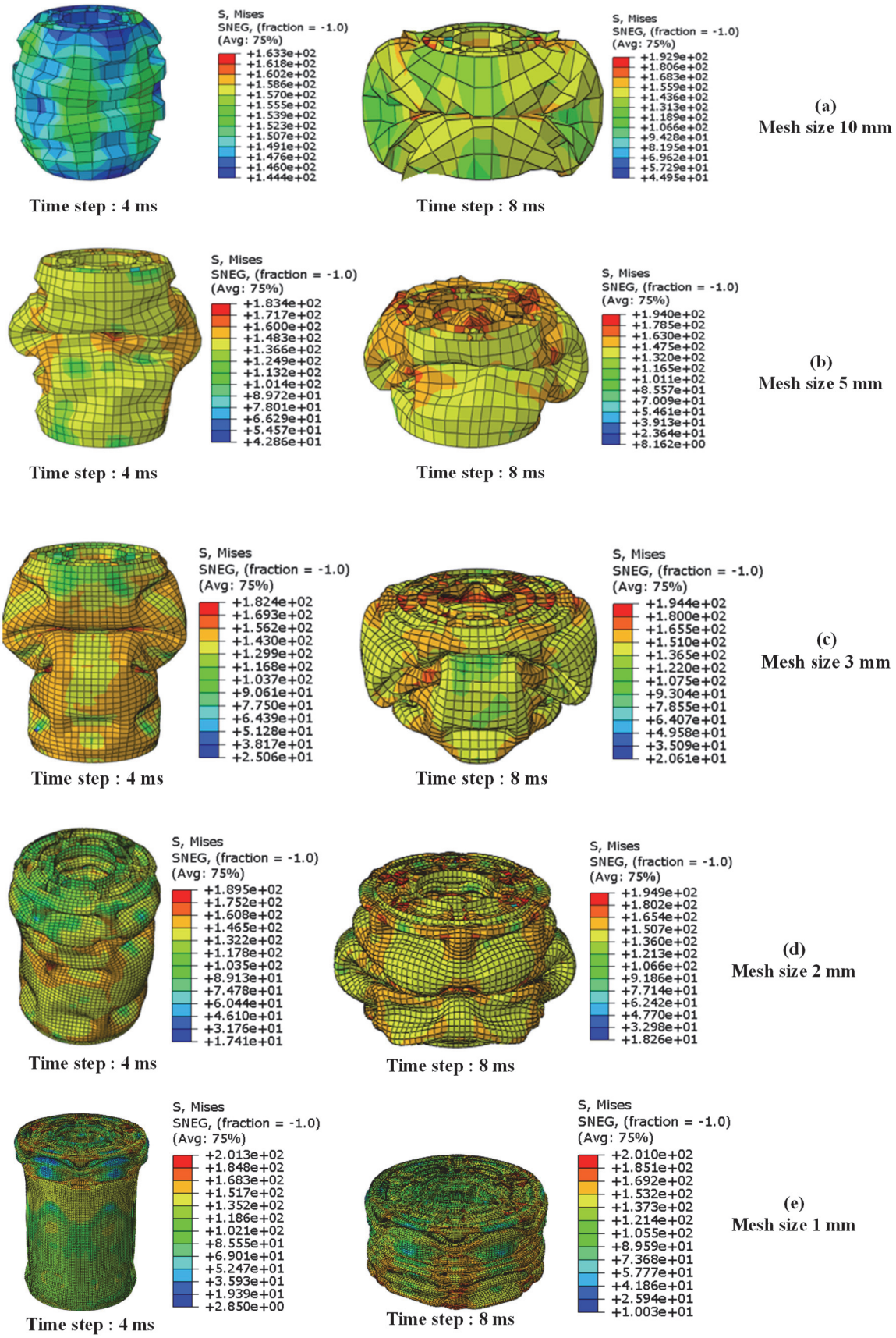

Figure 12: Progressive contour from different types of mesh size.

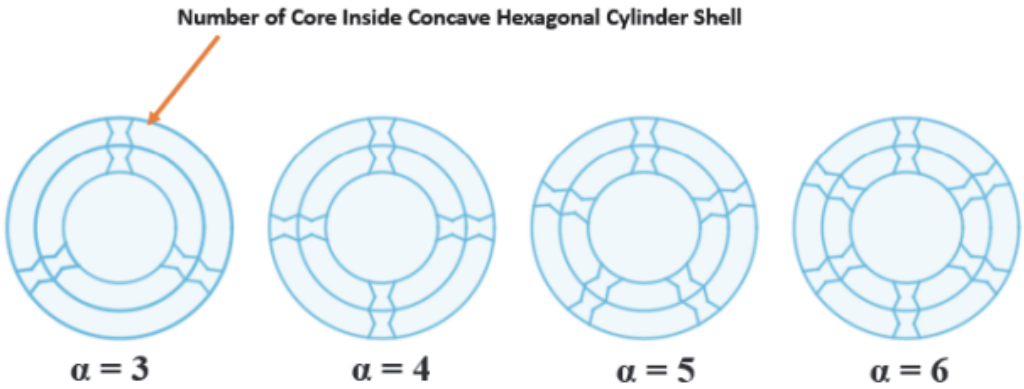

Figure 13: Variation of core (α) inside concave hexagonal cylinder shell.

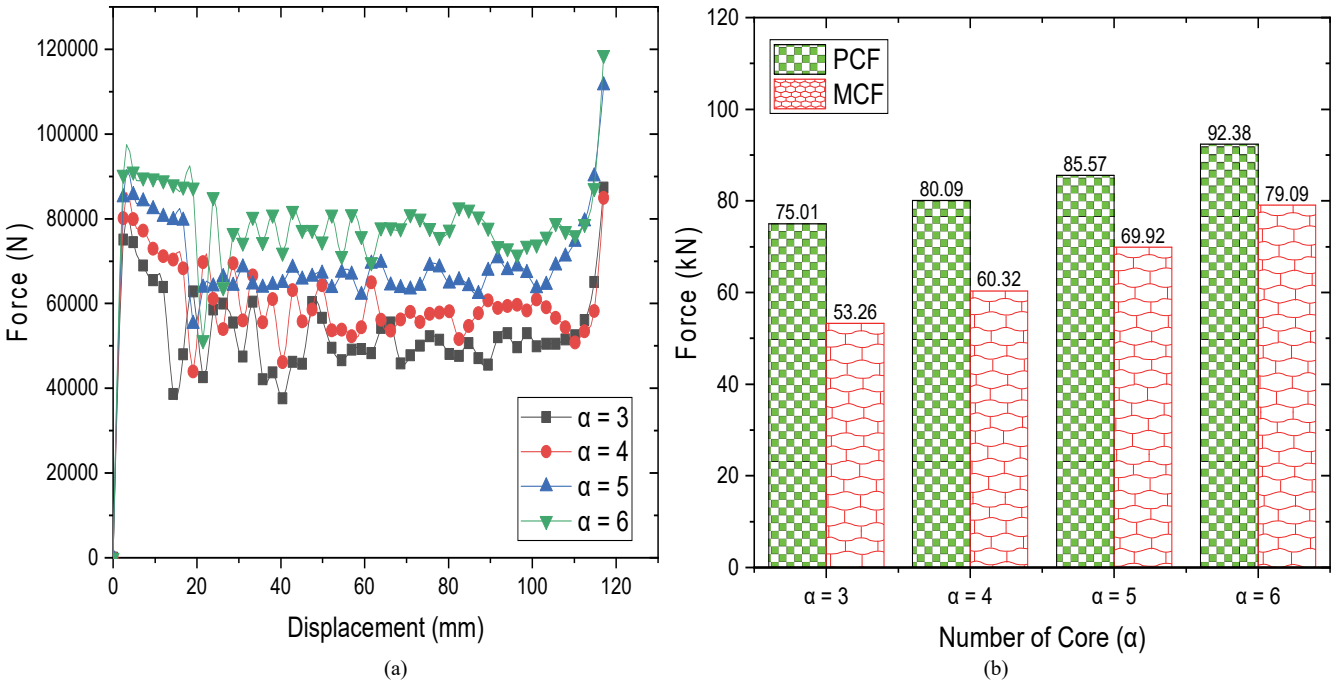

Figure 14: (a) Force – Displacement curve for variations of core (α); and (b) PCF and MCF for variations of core.

The highest PCF was obtained from α = 6, which was 92.38 kN, and the lowest was obtained from α = 3, which was 75.01 kN. The highest MCF value was obtained from α = 6, which was 79.09 kN, and the lowest was obtained from α = 3, which is 53.26 kN. Based on data in Fig. 14, the energy absorption by the cylindrical shell was greater as the number of cores increased, as detailed: α = 3 absorbed the energy of 6.23 kJ, α = 4 absorbed the energy of 7.06 kJ, 13.32% greater than α = 3, for α = 5 absorbed the energy of 8.18 kJ, 31.3% greater than α = 3, while for α = 6 absorbed the energy of 9.18 kJ or 47.35% greater than α = 3. From the above data, it can be concluded that the number of cores significantly affected the total energy absorption by the cylindrical shell. The stress progress contour for each number of cores can be observed in Fig. 16.

Effect of gradient thickness arrangement

In this section, all specimens had the same boundary condition, material, load, and mesh element type, applied with Cyl-1, except the shell element thickness. To investigate the gradient effect on the cylindrical shell as can be seen in Fig. 17a, we divided the cylindrical shell into three gradients with different thicknesses but with the value t = 1 mm or t = 2 mm and the same height, the height of each gradient was h = 50 mm. It is just that the sequence was different, after conducting a study it turned out that the gradient arrangement affected PCF and MCF. For example, the 1-1-2 thickness arrangement results in PCF and MCF were different from the 1-2-1 thickness arrangement. As can be seen in the graph in Fig. 17b, the gradient

arrangement had an effect on the final result obtained. It was classified into 2 categories: the arrangement consisting of t = 1 mm, two times, and the other category, namely the arrangement consisting of two times t = 2 mm.

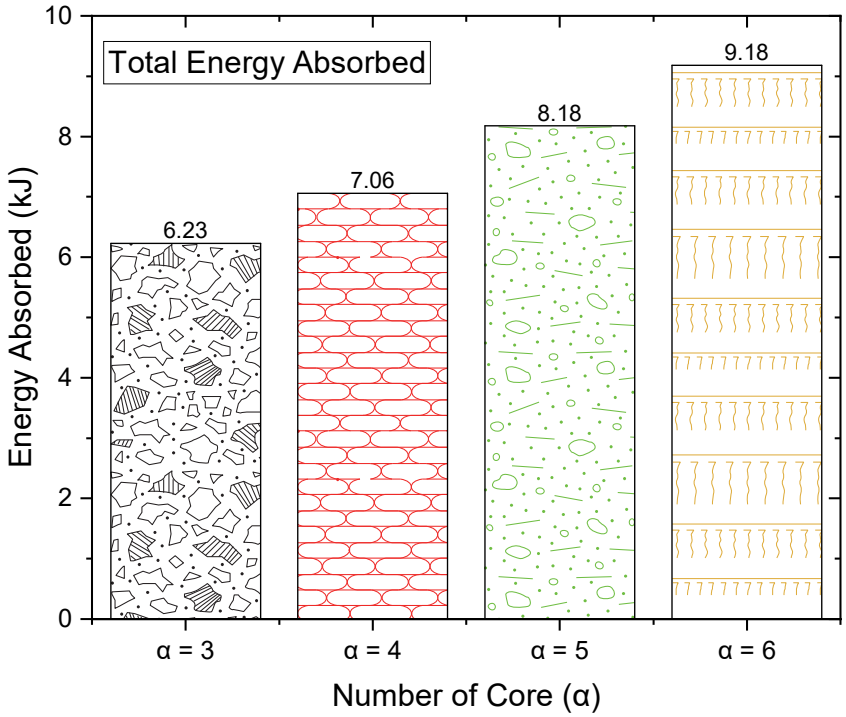

Figure 15: Energy absorption for each core (α).

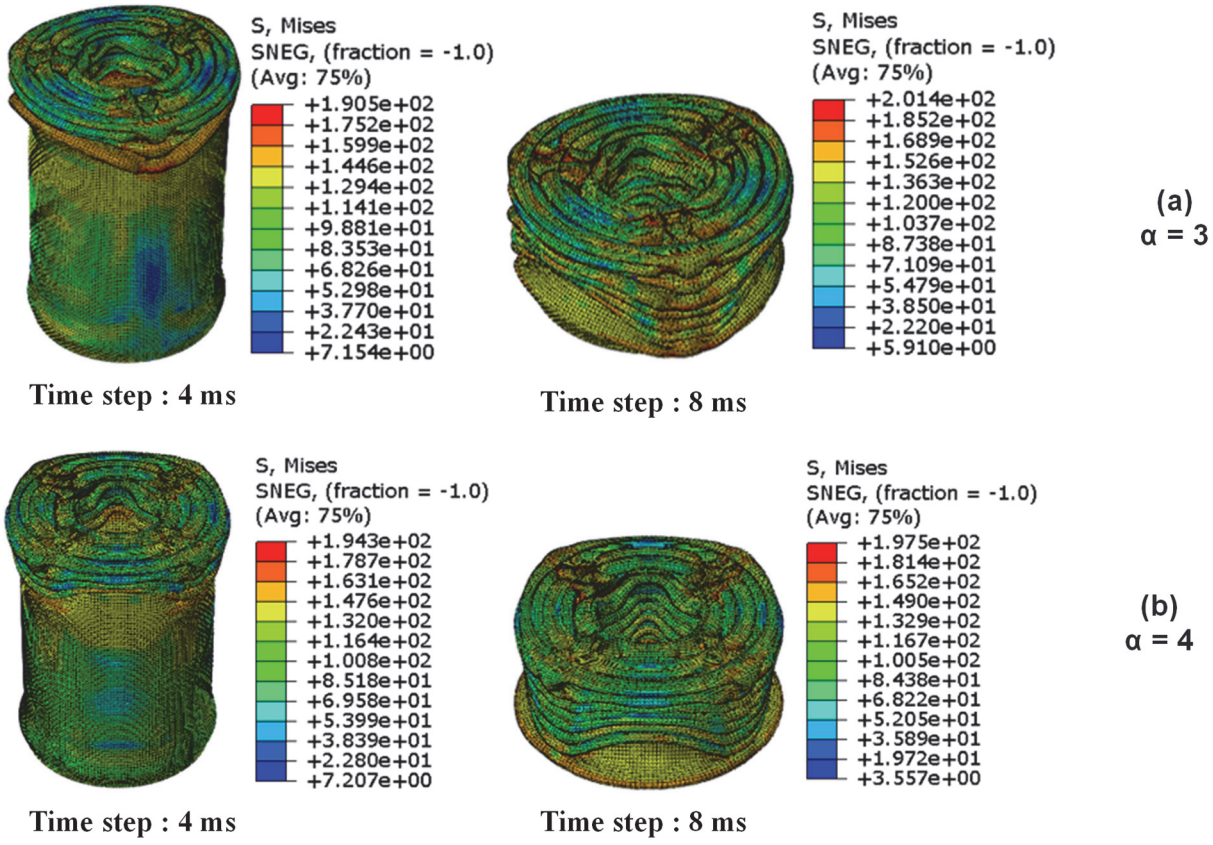

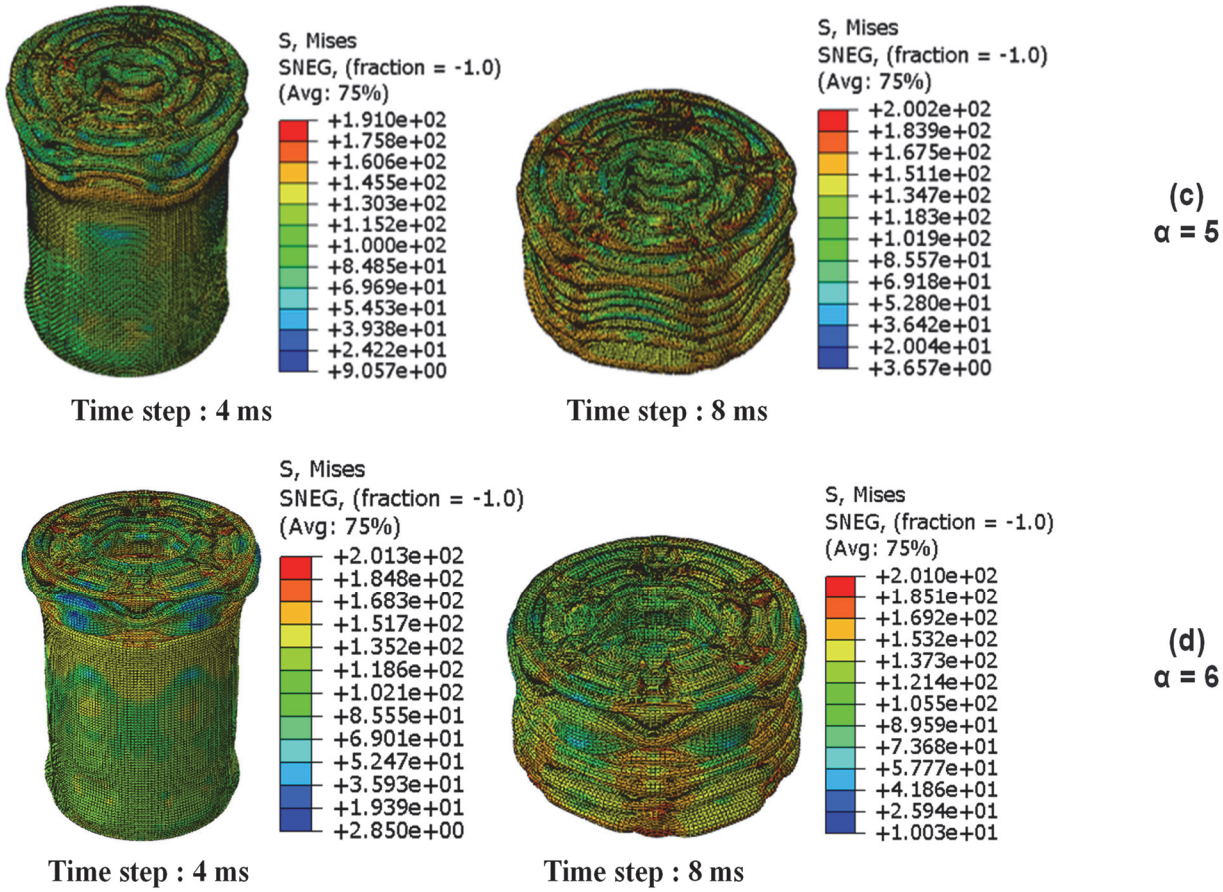

Figure 16: Progress of contour for each core specimen in 4 ms and 8 ms. (a) α = 3; (b) α = 4; (c) α = 5; and (d) α = 6.

After conducting a study of variations in arrangement thickness in Cyl-1, it can be seen in Fig. 17c that the phenomenon that occurred is in Category 1 with variations t = 1 mm, two times, that the PCF results would be greater when the gradient had thickness t = 2 mm (1-1- 2) with a value of 92.22 kN if it was placed at the bottom the PCF results would be greater than if t = 2 mm was placed above (2-1-1) with a value of 88.67 kN. The lowest result was obtained if t = 2 mm was placed in the middle with a value of 87.77 kN in the middle, while for MCF can be seen in Fig. 17d in category 1 the maximum result was obtained if t = 2 mm is placed at the top with a value of 115.88 kN, followed by placing t = 2 mm at the bottom with a value of 113.08 kN, the worst result was obtained if t = 2 mm was placed in the middle with a value of 93.74 kN.

In conclusion, the best results for the MCF value were obtained if the thicker gradient thickness was placed at the top than if the thicker gradient thickness was placed at the bottom, and the lowest results were obtained if a single gradient thickness was sandwiched by another gradient thickness with the different value of thickness. The results of this MCF will play a major role in the total energy absorbed value as shown in Fig. 20.

The same thing happened in Category 2 with a thickness of t = 2 mm, two times and t = 1 mm, one time which can be seen again in Fig. 17c that an effective PCF was obtained if t = 2 mm was placed on the bottom with a thickness of 2-1-2 PCF that occurred was 150.15 kN followed by a thickness of 1-2-2 of 149.53 kN, these two results were not much different compared to when t = 2 mm was placed on top and at the bottom, a wall with a smaller thickness t = 1 mm was placed, namely 2-2-1 with a value of 90.57 kN. For MCF in Category 2 which can be seen in Fig. 17d that the phenomenon that occurred is if a larger thickness was placed at the top (2-2-1) which had a value of 153.58 kN, the result would be greater than if a large thickness was placed at the bottom (1-2-2) with a value of 146.58 kN, the lowest MCF result if the middle part was placed with a different thickness from the top and bottom (2-1-2) with a value of 146.56.

For progress contours, it is depicted in Figs. 18 and 19. This shows that the thickness gradient affected the progress contour of the deformation where if a thicker thickness was placed on the part then the deformation occurred starting from the bottom to the top and vice versa if the gradient had a thicker thickness If the thick was placed on the bottom then the deformation process that occurred starts from the top to the bottom. So, it can be concluded that the part that has a lower gradient thickness will experience deformation first compared to a part with a thicker gradient thickness.

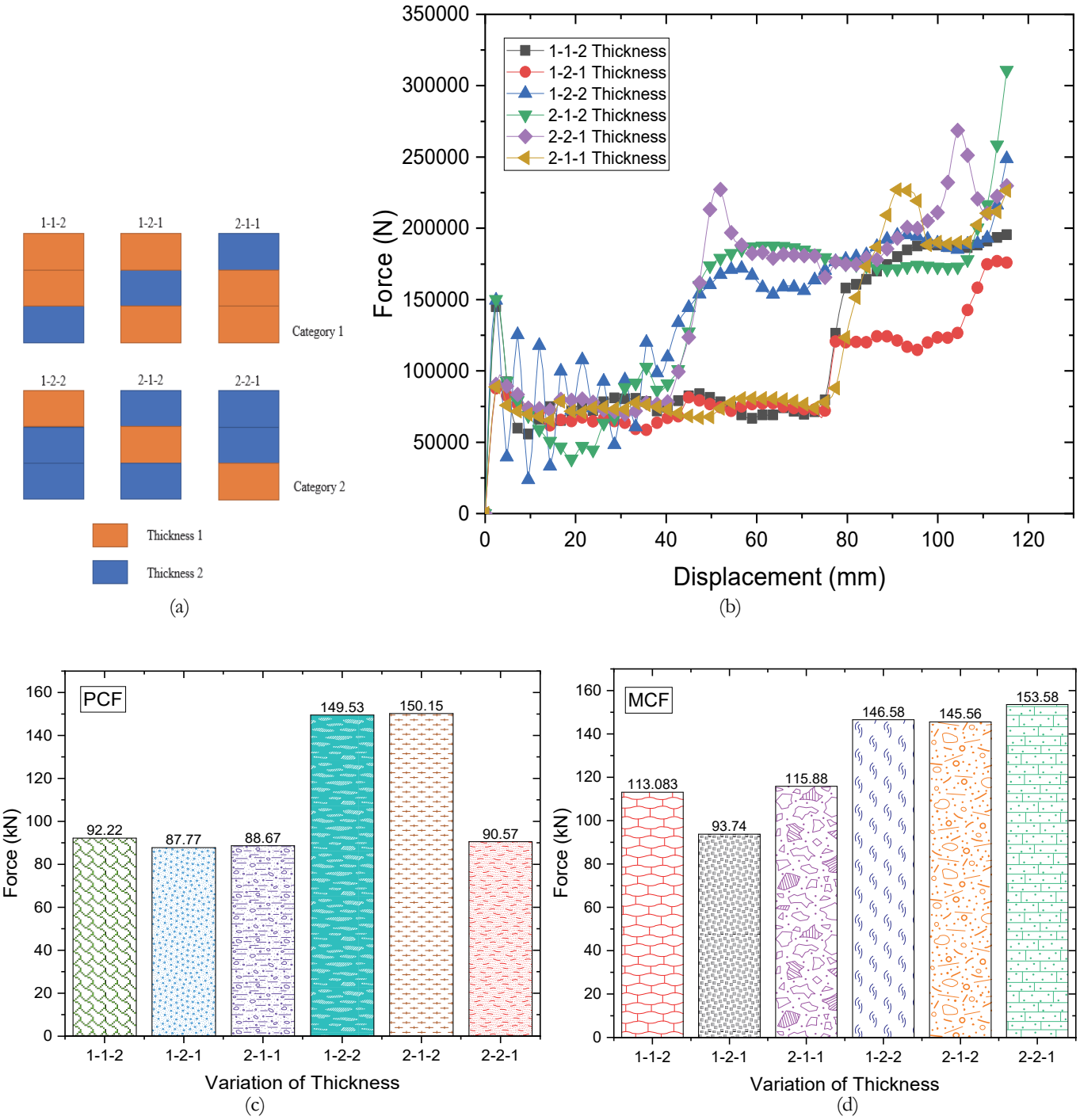

Figure 17: Variation of thickness configuration and results. (a) Thickness Configuration; (b) Force-Displacement result; (c) PCF result; and (d) MCF result.

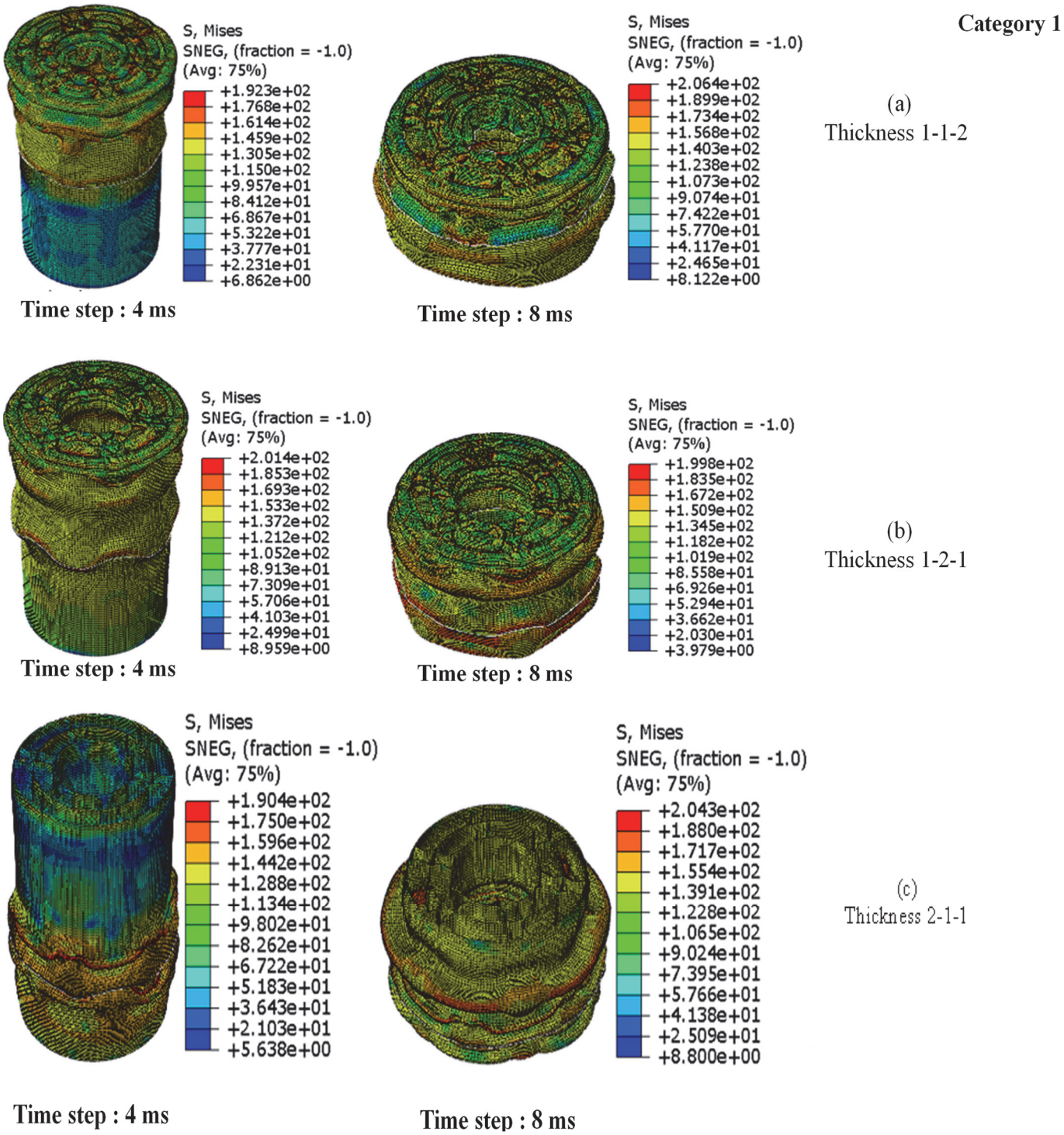

Figure 18: Different arrangement of thickness in Category 1.

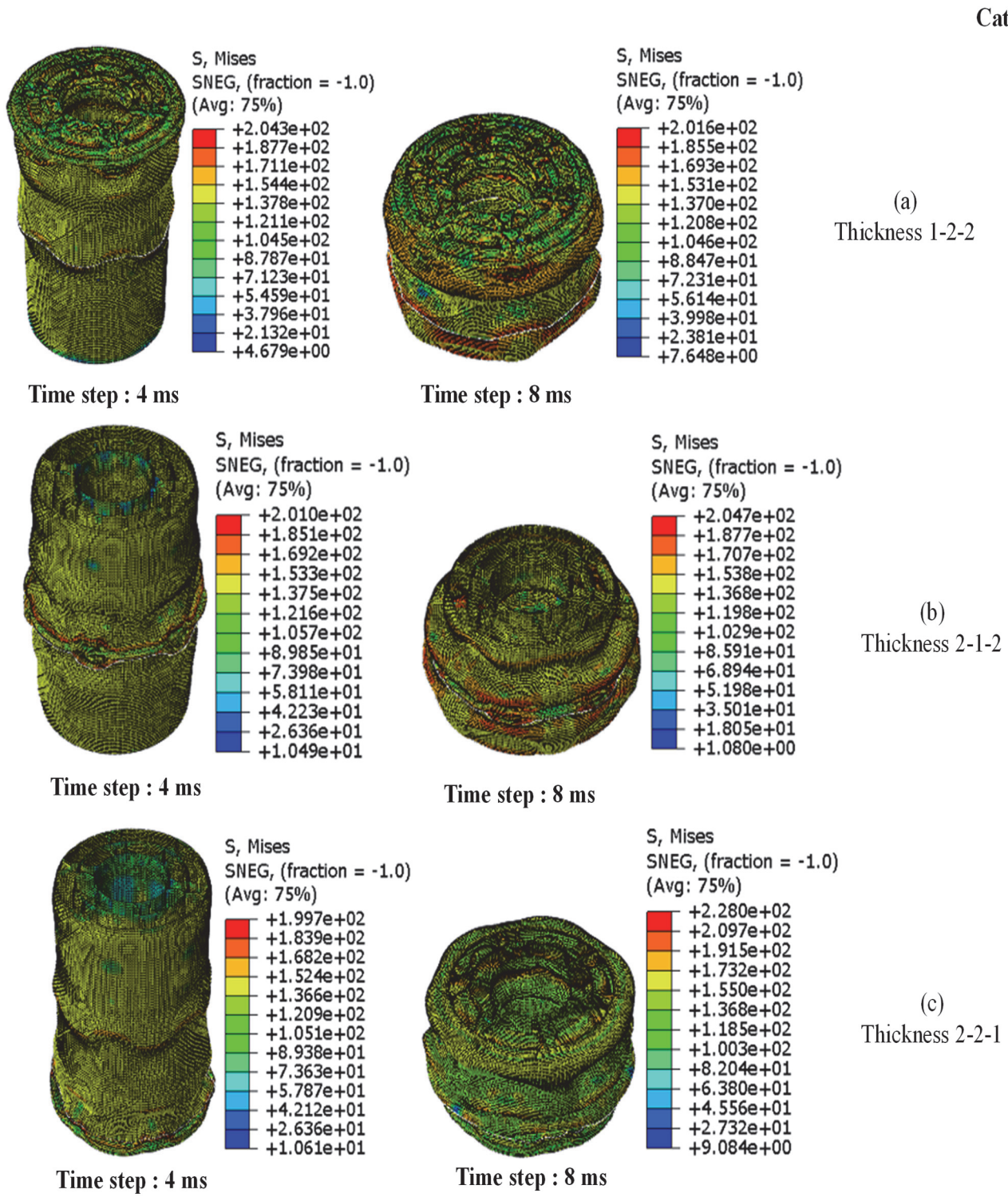

Figure 19: Different arrangement of thickness in category 2.

For total energy absorption, which can be observed in Fig. 20, the results similar to the MCF case will be found, namely if objects with a greater thickness were placed at the top in Category 1 and 2 in this case (2-1-1 and 2-2-1), the value will be greater than if the larger thickness was placed at the bottom in each category (1-1-2 and 1-2-2), and the lowest results in each category were found if identical thicknesses were placed at the top and bottom while the middle was placed a different

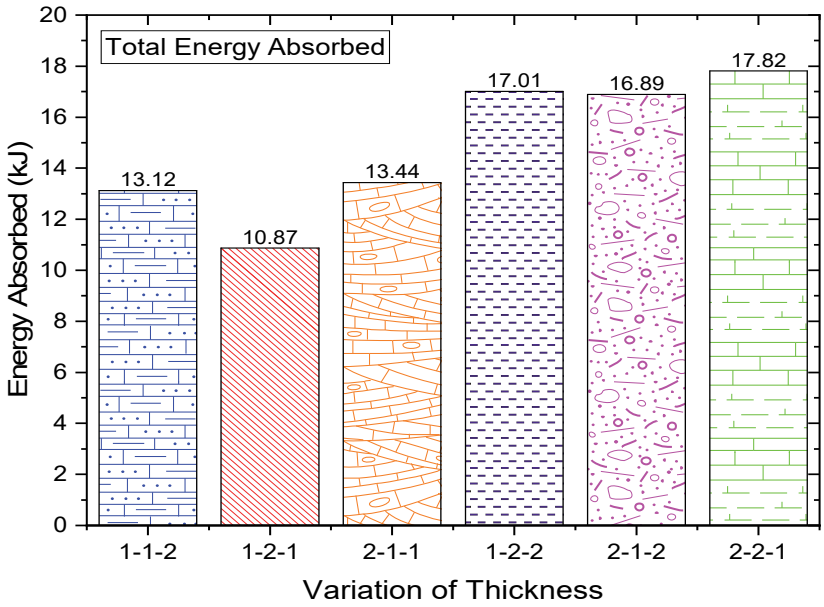

Figure 20: Energy absorption for each thickness arrangement.

Oblique compression

In this section, all specimens had the same boundary condition, material, load, and mesh element type, applied with Cyl-1, except the moving rigid wall angle. Fig. 21a shows a comparison of the force and energy absorption in Cyl-1 with a variety of different impact angles, the receiving angle varied from 0°, 10°, 20° and finally 30°. As an illustration, see Fig. 21b. Under 0° and 10° impact, the Cyl-1 structure showed excellent results in absorption energy compared to an angle of 20° or 30° which showed the ineffectiveness of the structure with that impact angle, marked by a decrease in force after the PCF point.

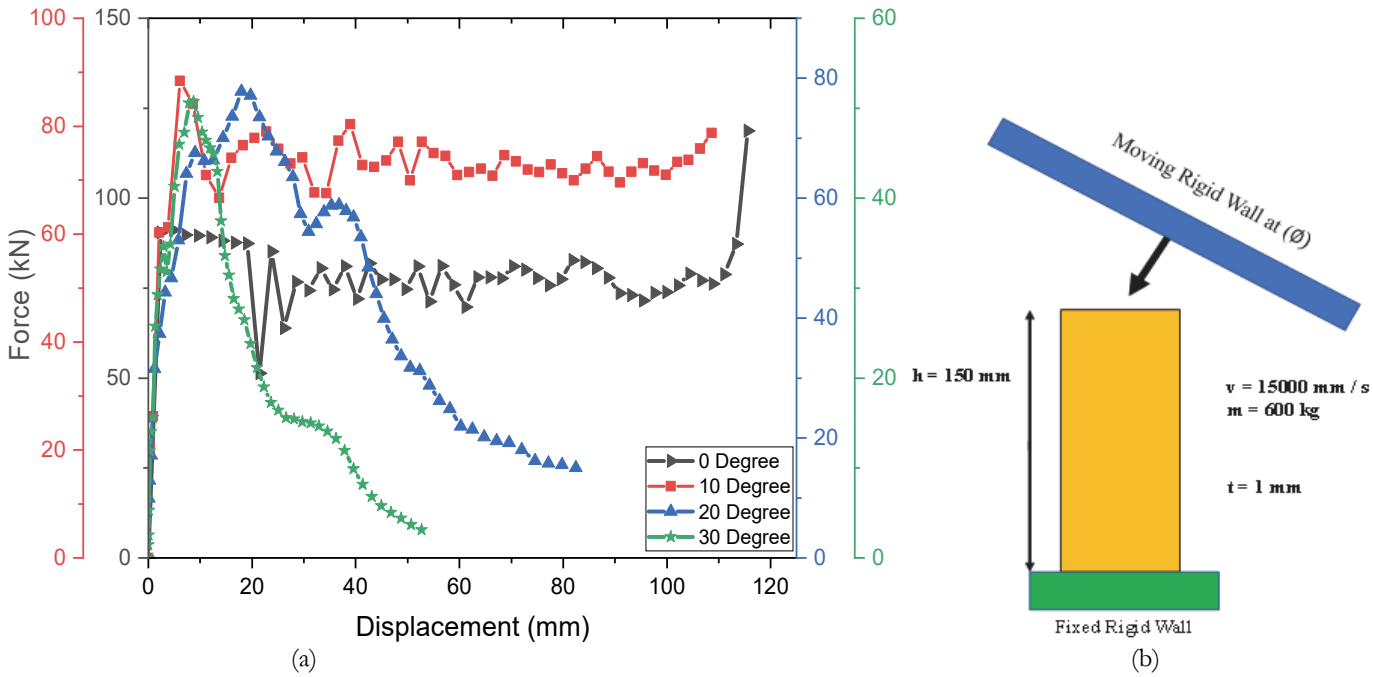

Figure 21: (a) Illustration of oblique impact in the cylindrical shell; and (b) Force – Displacement curve from 0° to 30°.

It can be seen from the progress contour experienced (Fig. 22) by the Cyl-1 specimen at various angles, that angles 0° and 10° had good absorption marked by the deformed object at the end of the compression process when (t = 8 ms), whereas when it was compressed at an angle of 20° and 30° the object was not effectively deformed, but tended to fall. This can be caused by the slippery surface of the object so that there was a slip that occurred between the collider and the specimen

wall, the greater the angle received, the greater the slip that will occur. This caused a decrease in the energy absorption by the specimen.

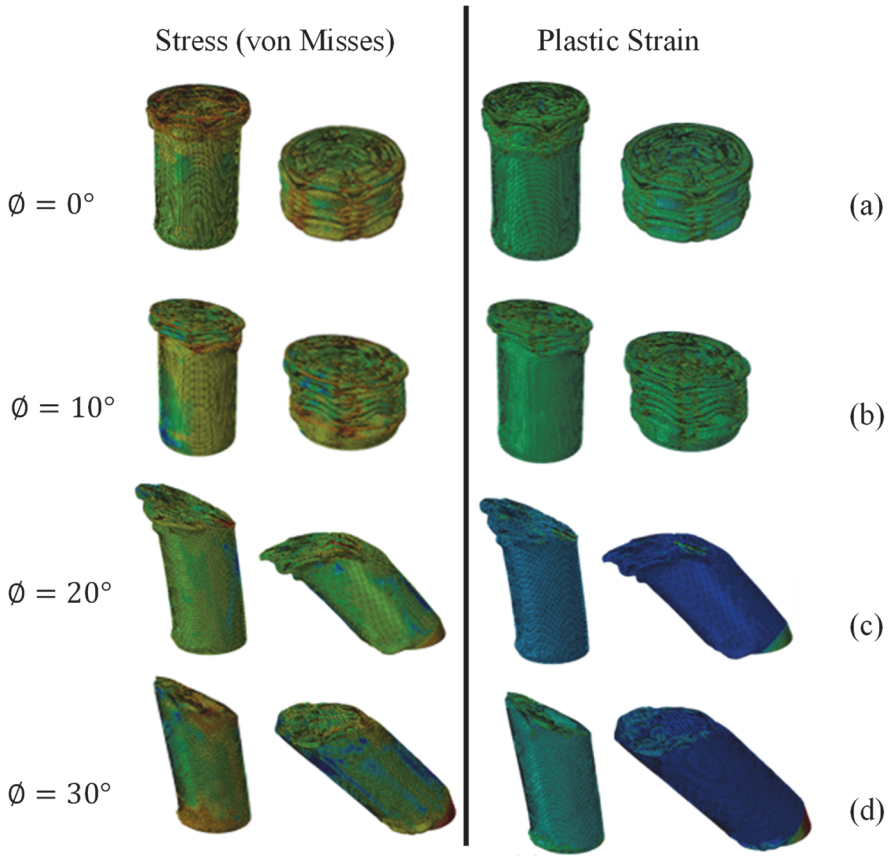

Figure 22: Deformation progress for each specimen during oblique compression.

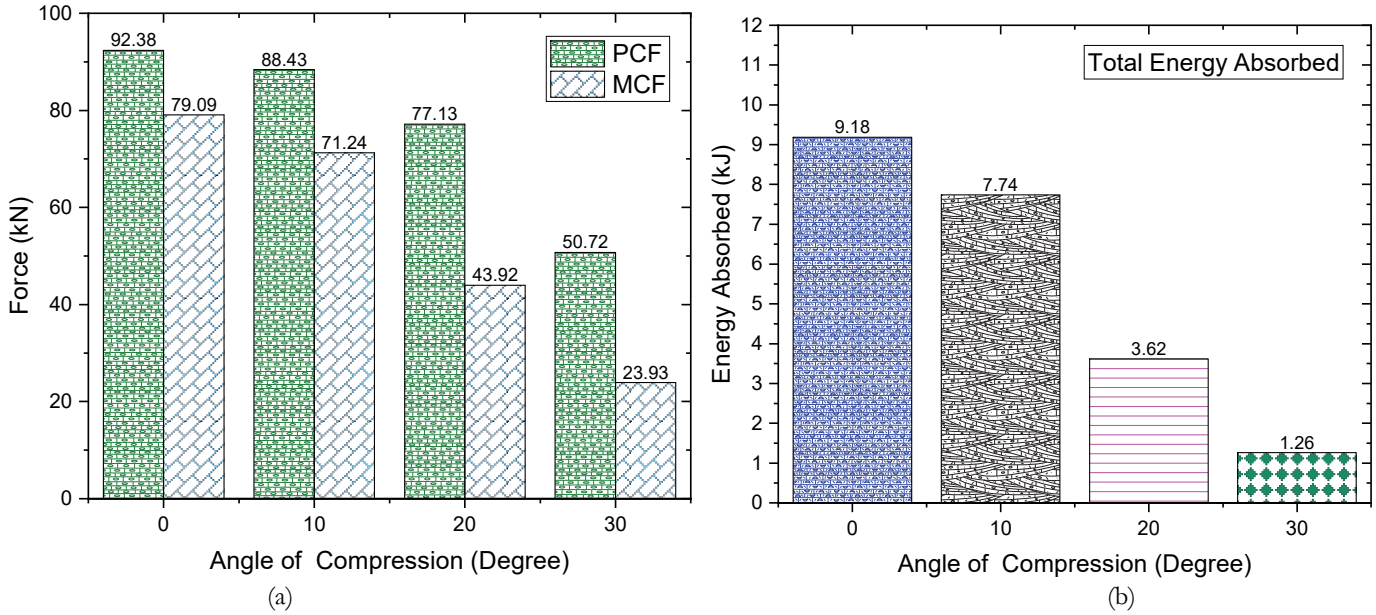

Figure 23: (a) Results of the PCF and MCF; and (b) Total energy absorption graph for each angle of compression.

Summarized results in Fig. 23 show that the largest Peak Crushing Force (PCF) was at an angle of 0°, and it decreased as the pressure angle increased pressure angle. For Total Energy absorption, the 0° angle effectively absorbed the force with a value of 9.18 kJ. For the 10° angle, it still had sufficient ability to absorb 7.74 kJ of energy or 84.31% from the axial angle.

In comparison, for the 20° angle, it absorbed as much as 3.62 kJ or 39.43% of the axial angle, and the last 30° angle which was only able to absorb as much energy as 1.26 kJ or only 13.72% of the axial angle.

CONCLUSIONS

Cylindrical shells with filler elements had better performance compared to ordinary hollow tubes. This can be observed by increasing the number of filler elements or cores (α). The more cores, the greater the energy absorption by the cylindrical shell. As an example, the comparison can be seen in the number of cores (α = 4), which absorbed the energy of 7.06 kJ. This result was 13.32% greater than the number of cores (α = 3), which was only able to absorb the energy of 6.23 kJ. The greater the number of elements, the smaller the energy absorption. At the number of elements 4,320, the value of energy absorption reached 22.03 kJ/kg. This value decreased as the number of elements increased. However, for elements 23,402, the energy absorption tended to stabilize at 4.5 kJ/kg. Mesh convergence was achieved at an energy absorption value of 2.87 kJ/kg with a total of 93,148 elements. The opposite occurred in displacements where the greater the number of elements, the greater the displacement that occurred. Mesh convergence was achieved when the displacement was 108.552 mm with the number of elements 96,148, with a mesh element size of t = 1 mm

Cylindrical with filler elements had a good crashworthiness ability if they hit at a small angle as an example, in this study, when the collision angle was 10° the energy absorption was 7.74 kJ,. This result was almost two times compared to the receiving angle of 20° which energy absorption was only 3.62 kJ. These results were influenced by several factors, and one of the main factors was the slip that occurred between the moving rigid wall and the specimen so that the energy absorption by the specimen was not optimal. The greater the oblique compression received, the less energy absorption by the object. For the gradient thickness arrangement with two different thickness categories and placed on one specimen which can be observed in the thickness arrangement study the results of each experiment were not similar and all differed. For example, the gradient thickness t = 2 mm (2-1-1) with the energy absorption was 13.44 kJ, compared to if t = 2 mm was placed at the bottom (1-1-2) with a value of 13.12 kJ. The two examples showed differences even though, in principle the arrangement consists of the same components, it was just that the order in which they were placed was different. For this thickness arrangement, objects tended to get a large energy absorption value if a thicker gradient thickness was placed on top, then followed by a larger gradient thickness placed at the bottom. Less optimal results were found if a smaller gradient thickness was placed in the middle and sandwiched with a greater thickness gradient at the top and bottom of the specimen.

We recommend further research to explore different multi-cell shapes or different geometries because the performance of multi-cell as crashworthiness is good, so further research is needed on the shape of multi-cell that is suitable for vehicles such as cars, ships, etc. We also suggest exploring the arrangement of gradient thickness in crashworthiness structures more deeply because gradient thickness has a big effect on energy absorption performance based on the arrangement or level of gradient thickness. In addition, further research is needed on the impact of this structure if it is hit at a certain speed that is more inclined to a certain speed experienced by the car so that the effectiveness of the crashworthiness structure can be further improved.

REFERENCES

[1] Ming, S., Zhou, C., Li, T., Song, Z., Wang, B. (2019). Energy absorption of thin-walled square tubes designed by kirigami approach, Int. J. Mech. Sci., 157–158, pp. 150–164, DOI: 10.1016/j.ijmecsci.2019.04.032.

[2] Li, Z., Yao, S., Ma, W., Xu, P., Che, Q. (2019). Energy-absorption characteristics of a circumferentially corrugated square tube with a cosine profile, Thin-Walled Struct., 135, pp. 385–99, DOI: 10.1016/j.tws.2018.11.028.

[3] Liu, Q., Liufu, K., Cui, Z., Li, J., Fang, J., Li, Q. (2020). Multiobjective optimization of perforated square CFRP tubes for crashworthiness, Thin-Walled Struct., 149, 106628, DOI: 10.1016/j.tws.2020.106628.

[4] Zhou, C., Ming, S., Xia, C., Wang, B., Bi, X., Hao, P., Ren, M. (2018). The energy absorption of rectangular and slotted windowed tubes under axial crushing, Int. J. Mech. Sci., 141, pp. 89–100, DOI: 10.1016/j.ijmecsci.2018.03.036.

[5] Xie, S., Chen, P., Wang, N., Wang, J., Du, X. (2021). Crashworthiness study of circular tubes subjected to radial extrusion under quasi-static loading, Int. J. Mech. Sci., 192, DOI: 10.1016/j.ijmecsci.2020.106128.

[6] Zhang, X.W., Yu, T.X. (2009). Energy absorption of pressurized thin-walled circular tubes under axial crushing, Int. J. Mech. Sci., 51(5), pp. 335–349, DOI: 10.1016/j.ijmecsci.2009.03.002.

[7] Wang, Z., Jin, X., Li, Q., Sun, G. (2020). On crashworthiness design of hybrid metal-composite structures, Int. J. Mech. Sci., 171, 105380, DOI: 10.1016/j.ijmecsci.2019.105380.

[8] Guillow, S.R., Lu, G., Grzebieta, R.H. (2001). Quasi-static axial compression of thin-walled circular alumunium tubes, Int. J. Mech. Sci., 43(9), pp. 2103-2123, DOI: 10.1016/S0020-7403(01)00031-5.
[9] Hao, W., Xie, J., Wang, F. (2017). Theoretical prediction of the progressive buckling and energy absorption of the sinusoidal corrugated tube subjected to axial crushing, Comput. Struct., 191, pp. 12–21, DOI: 10.1016/j.compstruc.2017.05.001.
[10] Hao, W., Xie, J.M., Wang, F., Liu, Z., Wang, Z. (2017). Analytical model of thin-walled corrugated tubes with sinusoidal patterns under axial impacting, Int. J. Mech. Sci., 128–129, pp. 1–16, DOI: 10.1016/j.ijmecsci.2017.03.033.
[11] Yao, S., Zhu, H., Liu, M., Li, Z., Xu, P. (2020). Energy absorption of origami tubes with polygonal cross-sections, Thin-Walled Struct., 157, 107013, DOI: 10.1016/j.tws.2020.107013.
[12] Yamashita, M., Gotoh, M., Sawairi, Y. (2003). Axial crush of hollow cylindrical structures with various polygonal cross-sections: Numerical simulation and experiment, J. Mater. Process. Technol., 140, pp. 59–64, DOI: 10.1016/S0924-0136(03)00821-5.
[13] Bai, C., Ma, Q., Gan, X., Zhou, T. (2021). Theoretical prediction model of mean crushing force of CFRP-Al hybrid circular tubes under axial compression, Polym. Compos., 42(10), pp. 5035–50, DOI: 10.1002/pc.26202.
[14] Wang, Z., Jin, X., Li, Q., Sun, G. (2020). On crashworthiness design of hybrid metal-composite structures, Int. J. Mech. Sci., 171, pp. 105380, DOI: 10.1016/j.ijmecsci.2019.105380.
[15] Ma, Q. hua., Dong, F., Gan, X. hui., Zhou, T. (2021). Effects of different interface conditions on energy absorption characteristics of Al/carbon fiber reinforced polymer hybrid structures for multiple loading conditions, Polym. Compos., 42(6), pp. 2838–2863, DOI: 10.1002/pc.26019.
[16] Fan, D., Qi-hua, M., Xue-hui, G., Tianjun, Z. (2021). Crashworthiness analysis of perforated metal/composite thin-walled structures under axial and oblique loading, Polym. Compos., 42(4), pp. 2019–2036, DOI: 10.1002/pc.25954.
[17] Lu, R., Liu, X., Chen, S., Xu, Z., Hu, X., Liu, L. (2019). Theoretical investigation on the crushing performances of Tailor Rolled Tubes with continuously varying thickness and material properties, Int. J. Mech. Sci., 151, pp. 106–117, DOI: 10.1016/j.ijmecsci.2018.09.012.
[18] Chisena, R.S., Chen, L., Shih, A.J. (2021). Finite element composite simplification modeling and design of the material extrusion wave infill for thin-walled structures, Int. J. Mech. Sci., 196, 106276, DOI: 10.1016/j.ijmecsci.2021.106276.
[19] Jia, Q., An, N., Ma, X., Zhou, J. (2021). Exploring the design space for nonlinear buckling of composite thin-walled lenticular tubes under pure bending, Int. J. Mech. Sci., 207, 106661, DOI: 10.1016/j.ijmecsci.2021.106661.
[20] Ren, Y., Jiang, H., Liu, Z. (2019). Evaluation of double- and triple-coupled triggering mechanisms to improve crashworthiness of composite tubes, Int. J. Mech. Sci., 157–158, pp. 1–12, DOI: 10.1016/j.ijmecsci.2019.04.024.
[21] Gao, Q., Liao, W.H. (2021). Energy absorption of thin walled tube filled with gradient auxetic structures-theory and simulation, Int. J. Mech. Sci., 201, 106475, DOI: 10.1016/j.ijmecsci.2021.106475.
[22] Deng, Y., Ren, Y., Fu, X., Jiang, H. (2021). Bionic-bamboo design for enhancing the crashworthiness of composite tube with groove trigger subjected to oblique load, Int. J. Mech. Sci., 206, 106635, DOI: 10.1016/j.ijmecsci.2021.106635.
[23] Gong, C., Bai, Z., Wang, Y., Zhang, L. (2021). On the crashworthiness performance of novel hierarchical multi-cell tubes under axial loading, Int. J. Mech. Sci., 206, pp. 106599, DOI: 10.1016/j.ijmecsci.2021.106599.
[24] Ha, N.S., Pham, T.M., Hao, H., Lu, G. (2021). Energy absorption characteristics of bio-inspired hierarchical multi-cell square tubes under axial crushing, Int. J. Mech. Sci., 201, pp. 106464, DOI: 10.1016/j.ijmecsci.2021.106464.
[25] Abada, M., Ibrahim, A. (2020). Hybrid multi-cell thin-walled tubes for energy absorption applications: Blast shielding and crashworthiness, Compos. Part B Eng., 183, 107720, DOI: 10.1016/j.compositesb.2019.107720.
[26] Li, Z., Ma, W., Xu, P., Yao, S. (2020). Crashworthiness of multi-cell circumferentially corrugated square tubes with cosine and triangular configurations, Int. J. Mech. Sci., 165, DOI: 10.1016/j.ijmecsci.2019.105205.
[27] Liu, H., Chng, Z.X.C., Wang, G., Ng, B.F. (2021). Crashworthiness improvements of multi-cell thin-walled tubes through lattice structure enhancements, Int. J. Mech. Sci., 210, 106731, DOI: 10.1016/j.ijmecsci.2021.106731.
[28] Tran, T.N., Baroutaji, A., Estrada, Q., Arjunan, A., Le, H.S., Thien, N.P. (2021). Crashworthiness analysis and optimization of standard and windowed multi-cell hexagonal tubes, Struct. Multidiscip. Optim., 63(5), pp. 2191–2209, DOI: 10.1007/s00158-020-02794-y.
[29] Abdullahi, H.S., Gao, S. (2020). A novel multi-cell square tubal structure based on Voronoi tessellation for enhanced crashworthiness, Thin-Walled Struct., 150(August 2019), 106690, DOI: 10.1016/j.tws.2020.106690.
[30] Tran, T.N. (2017). Crushing analysis under multiple impact loading cases for multi-cell triangular tubes, Thin-Walled Struct., 113, pp. 262–272, DOI: 10.1016/j.tws.2017.01.013.
[31] Tran, T.N., Baroutaji, A. (2018). Crashworthiness optimal design of multi-cell triangular tubes under axial and oblique impact loading, Eng. Fail. Anal., 93, pp. 241–256, DOI: 10.1016/j.engfailanal.2018.07.003.

[32] Kim, H.S. (2002). New extruded multi-cell alumunium profile for maximum crash energy absorption and weight efficiency, Thin-Walled Struct., 40(4), pp. 311–327, DOI: 10.1016/S0263-8231(01)00069-6.
[33] Vinayagar, K., Senthil Kumar, A. (2017). Crashworthiness analysis of double section bi-tubular thin-walled structures, Thin-Walled Struct., 112, pp. 184–193, DOI: 10.1016/j.tws.2016.12.008.
[34] Sun, G., Liu, T., Fang, J., Steven, G.P., Li, Q. (2018). Configurational optimization of multi-cell topologies for multiple oblique loads, Struct. Multidiscip. Optim., 57(2), pp. 469–488, DOI: 10.1007/s00158-017-1839-5.
[35] [35] Statista Research Depatrtment (2023). Number of deaths in road accidents in Italy 2020, by region/Available at: https://www.statista.com/statistics/914470/number-of-deaths-in-road-accidents-in-italy-by-region/
[36] Rogala, M., Gajewski, J., Ferdynus, M. (2020). The effect of geometrical non-linearity on the crashworthiness of thin-walled conical energy-absorbers, Materials, 13(21), pp. 1–18, DOI: 10.3390/ma13214857.
[37] Tarlochan, F., Samer, F., Hamouda, A.M.S., Ramesh, S., Khalid, K. (2013). Design of thin wall structures for energy absorption applications: Enhancement of crashworthiness due to axial and oblique impact forces, Thin-Walled Struct., 71, pp. 7–17, DOI: 10.1016/j.tws.2013.04.003.
[38] Abramowicz, W., Jones, N. (1984). Dynamic axial crushing of circular tubes, Int. J. Impact Eng., 2(3), pp. 263–281, DOI: 10.1016/0734-743X(84)90010-1.
[39] Boria, S., Scattina, A., Belingardi, G. (2018). Axial crushing of metal-composite hybrid tubes: Experimental analysis, Procedia Struct. Integr., 8, pp. 102–117, DOI: 10.1016/j.prostr.2017.12.012.
[40] Liang, H., Hao, W., Sun, H., Pu, Y., Zhao, Y., Ma, F. (2022). On design of novel bionic bamboo tubes for multiple compression load cases, Int. J. Mech. Sci., 218, 107067, DOI: 10.1016/j.ijmecsci.2022.107067.
[41] Dassault Systèmes Simulia Corp. (2013). Damage and failure for fiber-reinforced composites, Abaqus 6.13 Anal. User's Guid. Vol. III Mater., III, pp. 1–4
[42] Wiśniewski, K., Kołakowski, P. (2003). The effect of selected parameters on ship collision results by dynamic FE simulations, Finite Elem. Anal. Desig., 39(10), pp. 985-1006, DOI: 10.1016/S0168-874X(02)00143-9.
[43] Prabowo, A.R., Muttaqie, T., Sohn, J.M., Harsritanto, B.I.R. (2019). Investigation on structural component behaviours of double bottom arrangement under grounding accidents, Theo. Appl. Mech. Lett., 9(1), pp. 50–59, DOI: 10.1016/j.taml.2019.01.010.
[44] Cao, B., Bae, D.-M., Sohn, J.-M., Prabowo, A.R., Chen, T.H., Li, H. (2016). Numerical analysis for damage characteristics caused by ice collision on side structure, Proc. Int. Conf. Offshore Mech. Arctic Eng. - OMAE, 8, V008T07A019, DOI: 10.1115/OMAE2016-54727.
[45] Prabowo, A.R., Bae, D.M., Sohn, J.M. (2019). Comparing structural casualties of the Ro-Ro vessel using straight and oblique collision incidents on the car deck, J. Mar. Sci. Eng., 7(6), 183, DOI: 10.3390/jmse7060183.
[46] Do, Q.T., Muttaqie, T., Nhut, P.T., Vu, M.T., Khoa, N.D., Prabowo, A.R. (2022). Residual ultimate strength assessment of submarine pressure hull under dynamic ship collision, Ocean Eng., 266, 112951, DOI: 10.1016/j.oceaneng.2022.112951.
[47] Prabowo, A.R., Sohn, J.M. (2019). Nonlinear dynamic behaviors of outer shell and upper deck structures subjected to impact loading in maritime environment. Curve. Layer. Struc., 6(1), pp. 146–160, DOI: 10.1515/cls-2019-0012.
[48] Prabowo, A.R., Byeon, J.H., Cho, H.J., Sohn, J.M., Bae, D.M., Cho, J.H. (2018). Impact phenomena assessment: Part I-Structural performance of a tanker subjected to ship grounding at the Arctic, MATEC Web Conf., 159, 02061, DOI: 10.1051/matecconf/201815902061.
[49] Prabowo, A.R., Bahatmaka, A., Cho, J.H., Sohn, J.M., Samuel, S., Cao, B. (2016). Analysis of structural crashworthiness on a non-ice class tanker during stranding accounting for the sailing routes, Maritime Transportation and Harvesting of Sea Resources, 1, pp. 645–654.
[50] Prabowo, A.R., Sohn, J.M., Bae, D.M., Cho, J.H. (2018). Estimating structure response and progressive failure of a ship hull under side-bow collisions, Tehnicki Vjesnik, 25(5), pp. 1513–1522, DOI: 10.17559/TV-20170215113629.
[51] Prabowo, A.R., Bahatmaka, A., Sohn, J.M. (2020). Crashworthiness characteristic of longitudinal deck structures against identified accidental action in marine environment: a study case of ship–bow collision, J. Braz. Soc. Mech. Sci. Eng., 42(11), 584, DOI: 10.1007/s40430-020-02662-2.
[52] Prabowo, A.R., Cho, H.J., Lee, S.G., Baek, S.J., Byeon, J.H., Be, D.M., Sohn, J.M., Harsritanto, B.I. (2018). Evaluating structural crashworthiness and progressive failure of double hull tanker under accidental grounding: Bottom raking case. Open Eng., 8(1), pp. 193–204, DOI: 10.1515/eng-2018-0024.
[53] Jafarzadeh-Aghdam, N., Schröder, K.U. (2022). Mechanism of reproducible axial impact of square crash boxes, Thin-Walled Struct., 176(January), pp. 109062, DOI: 10.1016/j.tws.2022.109062.
[54] Zarei, H.R., Kröger, M. (2008). Optimization of the foam-filled aluminum tubes for crush box application, Thin-Walled Struct., 46(2), pp. 214–221, DOI: 10.1016/j.tws.2007.07.016.